Theses and Dissertations | 1. Thesis and Dissertation Collection, all items

2009

Initiation mechanisms of low-loss swept-ramp obstacles for deflagration to detonation transition in pulse detonation combustors

Myers, Charles B.

Monterey, California. Naval Postgraduate School

http://hdl.handle.net/10945/4477

NAVAL POSTGRADUATE SCHOOL

MONTEREY, CALIFORNIA

THESIS

INITIATION MECHANISMS OF LOW-LOSS
SWEPT-RAMP OBSTACLES FOR DEFLAGRATION TO
DETONATION TRANSITION IN PULSE DETONATION
COMBUSTORS

by

Charles B. Myers IV

December 2009

Thesis Advisor: Christopher M. Brophy
Second Reader: Garth V. Hobson

Approved for public release; distribution is unlimited

THIS PAGE INTENTIONALLY LEFT BLANK

REPORT DOCUMENTATION PAGE		Form Approved OMB No. 0704-0188

Public reporting burden for this collection of information is estimated to average 1 hour per response, including the time for reviewing instruction, searching existing data sources, gathering and maintaining the data needed, and completing and reviewing the collection of information. Send comments regarding this burden estimate or any other aspect of this collection of information, including suggestions for reducing this burden, to Washington headquarters Services, Directorate for Information Operations and Reports, 1215 Jefferson Davis Highway, Suite 1204, Arlington, VA 22202-4302, and to the Office of Management and Budget, Paperwork Reduction Project (0704-0188) Washington DC 20503.

1. AGENCY USE ONLY *(Leave blank)*	2. REPORT DATE December 2009	3. REPORT TYPE AND DATES COVERED Master's Thesis
4. TITLE AND SUBTITLE Initiation Mechanisms of Low-loss Swept-ramp Obstacles for Deflagration to Detonation Transition in Pulse Detonation Combustors		**5. FUNDING NUMBERS** **N0001409WR20022**
6. AUTHOR(S) Charles B. Myers IV		
7. PERFORMING ORGANIZATION NAME(S) AND ADDRESS(ES) Naval Postgraduate School Monterey, CA 93943-5000		**8. PERFORMING ORGANIZATION REPORT NUMBER**
9. SPONSORING /MONITORING AGENCY NAME(S) AND ADDRESS(ES) Office of Naval Research (ONR) Code 33 Ballstone Tower One 800 N. Quincy St Arlington, VA 22203-1995		**10. SPONSORING/MONITORING AGENCY REPORT NUMBER**
11. SUPPLEMENTARY NOTES The views expressed in this thesis are those of the author and do not reflect the official policy or position of the Department of Defense or the U.S. Government.		
12a. DISTRIBUTION / AVAILABILITY STATEMENT Approved for public release; distribution is unlimited		**12b. DISTRIBUTION CODE** A

13. ABSTRACT (maximum 200 words)

In order to enhance the performance of pulse detonation combustors (PDCs), an efficient deflagration-to-detonation transition (DDT) process is critical to maintain the thermodynamic benefits of detonation-based combustion systems and enable their use as future propulsion or power generation systems. The DDT process results in the generation of detonation and can occur independently, but the required length is excessive in many applications and also limits the frequency of repeatability. Historically, obstacles have been used to reduce the required distance for DDT, but often result in a significant total pressure loss that lessens the delivered efficiency advantages of PDCs. This thesis evaluated various swept-ramp obstacle configurations to accelerate DDT in a single event PDC. Computer simulations were used to investigate the three-dimensional disturbances caused by various swept-ramp configurations. Experimental tests were conducted using various configurations that measured combustion shockwave speed and flame front interactions with the swept-ramp obstacles. Detonation was verified across the instrumented section through high-frequency pressure transducers, and experimental data proved that swept-ramp obstacles successfully accelerate the DDT process with minimal pressure losses.

14. SUBJECT TERMS Pulse Detonation Combustors, PDC, Pulse Detonation Engines, PDE, PDE Ignition, PDE Initiation, Low-Loss Obstacles, Ramp, Swept Ramp, DDT, DDT Initiation			**15. NUMBER OF PAGES** 113
			16. PRICE CODE
17. SECURITY CLASSIFICATION OF REPORT Unclassified	**18. SECURITY CLASSIFICATION OF THIS PAGE** Unclassified	**19. SECURITY CLASSIFICATION OF ABSTRACT** Unclassified	**20. LIMITATION OF ABSTRACT** UU

NSN 7540-01-280-5500

Standard Form 298 (Rev. 2-89)
Prescribed by ANSI Std. 239-18

THIS PAGE INTENTIONALLY LEFT BLANK

INITIATION MECHANISMS OF LOW-LOSS SWEPT-RAMP OBSTACLES FOR DEFLAGRATION TO DETONATION TRANSITION IN PULSE DETONATION COMBUSTORS

Charles B. Myers IV
Lieutenant, United States Navy
B.S., Auburn University, 2003

Submitted in partial fulfillment of the
requirements for the degree of

MASTER OF SCIENCE IN ASTRONAUTICAL ENGINEERING

from the

NAVAL POSTGRADUATE SCHOOL
December 2009

Author: Charles B. Myers IV

Approved by: Christopher M. Brophy
                 Thesis Advisor

                 Garth V. Hobson
                 Second Reader

                 Knox T. Millsaps
                 Chairman, Department of Mechanical and Astronautical
                 Engineering

iii

THIS PAGE INTENTIONALLY LEFT BLANK

ABSTRACT

In order to enhance the performance of pulse detonation combustors (PDCs), an efficient deflagration-to-detonation transition (DDT) process is critical to maintain the thermodynamic benefits of detonation-based combustion systems and enable their use as future propulsion or power generation systems. The DDT process results in the generation of detonation and can occur independently, but the required length is excessive in many applications and also limits the frequency of repeatability. Historically, obstacles have been used to reduce the required distance for DDT, but often result in a significant total pressure loss that lessens the delivered efficiency advantages of PDCs. This thesis evaluated various swept-ramp obstacle configurations to accelerate DDT in a single event PDC. Computer simulations were used to investigate the three-dimensional disturbances caused by various swept-ramp configurations. Experimental tests were conducted using various configurations that measured combustion shockwave speed and flame front interactions with the swept-ramp obstacles. Detonation was verified across the instrumented section through high-frequency pressure transducers, and experimental data proved that swept-ramp obstacles successfully accelerate the DDT process with minimal pressure losses.

THIS PAGE INTENTIONALLY LEFT BLANK

TABLE OF CONTENTS

THIS PAGE INTENTIONALLY LEFT BLANK

LIST OF FIGURES

THIS PAGE INTENTIONALLY LEFT BLANK

LIST OF TABLES

THIS PAGE INTENTIONALLY LEFT BLANK

LIST OF ABBREVIATIONS, ACRONYMS, AND SYMBOLS

Symbol	Description	Units
C-J	Chapman-Jouguet	
CAD	Computer-Aided Design	
CCD	Charge-Coupled Device	
CFD	Computational Fluid Dynamics	
CMOS	Complementary Metal–Oxide–Semiconductor	
CPU	Central Processing Unit	
CEQUEL	Chemical Equilibrium in Excel	
DDT	Deflagration-To-Detonation Transition	
NI	National Instruments	
NPS	Naval Postgraduate School	
PDC	Pulse Detonation Combustor	
PDE	Pulse Detonation Engine	
RAM	Random Access Memory	
RDT	Research, Design and Test	
RPL	Rocket Propulsion Laboratory	
STP	Standard Temperature and Pressure	
TKE	Turbulence Kinetic Energy	$[\frac{m^2}{s^2}]$
USB	Universal Serial Bus	
VI	Virtual Instrument	
VIS	Variable Ignition System	
ZND	Zeldovich–Neumann–Döring	
A	Area	
C	carbon	
C_2H_4	ethylene	
c	speed of sound	$[\frac{m}{s}]$

c_P	constant pressure coefficient of specific heat $[\dfrac{J}{kg \cdot K}]$	
cm	centimeter	
f	fuel-to-air ratio	
GB	gigabyte	
GHz	gigahertz	
g	gravitational constant	
H	hydrogen	
K	Kelvin	
kg	kilogram	
MHz	megahertz	
m	meter	
mm	millimeter	
M	Mach number	
MB	Megabyte	
Mb	Megabit	
$\dot{m}$	mass flow rate	$[\dfrac{kg}{s}]$
$\dot{m}_f$	mass flow rate of fuel	$[\dfrac{kg}{s}]$
$\dot{m}_a$	mass flow rate of air	$[\dfrac{kg}{s}]$
$\dot{m}_{tot}$	total mass flow rate	$[\dfrac{kg}{s}]$
N	nitrogen	
O	oxygen	
p	pressure	
psi	pounds per square inch	
psig	pounds per square inch gage	
P-v	pressure-specific volume	
q	specific heat	

R	specific gas constant	
s	second	
s	specific entropy	$[\dfrac{J}{kg \cdot K}]$
t	time	
T	temperature	
u	velocity	$[\dfrac{m}{s}]$
V_{det}	Detonation Velocity	
v	velocity	$[\dfrac{m}{s}]$
ϕ	equivalence ratio	
γ	specific heat ratio	
ρ	density	$[\dfrac{kg}{m}]$

THIS PAGE INTENTIONALLY LEFT BLANK

ACKNOWLEDGMENTS

THIS PAGE INTENTIONALLY LEFT BLANK

I.   INTRODUCTION

Current propulsion technologies such as turbojet/turbofans and rockets have reached a maturity level where future development will not likely produce significant gains in thermodynamic efficiency and performance. Various propulsion technologies are capable of high performance and practical thermodynamic efficiency in a specific range of flight Mach number. None of the current air breathing propulsion systems have the capability to maintain their high performance level and efficiency over a large range of speed. Pulse Detonation Combustion is a technology being explored in advanced future propulsion concepts that will allow higher performance due to the increase in the thermodynamic efficiency of the engine cycle, thus increasing the range of the propulsion system. One of the critical hurdles to achieving detonation-based propulsion systems is creating an efficient deflagration-to-detonation process. Understanding the initiation mechanisms for an efficient detonation process is vital in overcoming the current technical challenges associated with implementing this type of propulsion. Current research at the Naval Postgraduate School (NPS) along with several other institutions are attempting to overcome the technical hurdles that are currently inhibiting the implementation of this advanced propulsion system.

The primary advantage offered by pulse detonation engines (PDEs) is the high efficiency in a nearly constant-volume combustion process. Under Mach 5, specific impulses of PDEs have been theorized to be greater than most supersonic air-breathing engines currently in use, with the exception of advanced turbofan/turbojet engines. Figure 1 shows various propulsion concepts and their specific impulse over a range of flight Mach numbers.
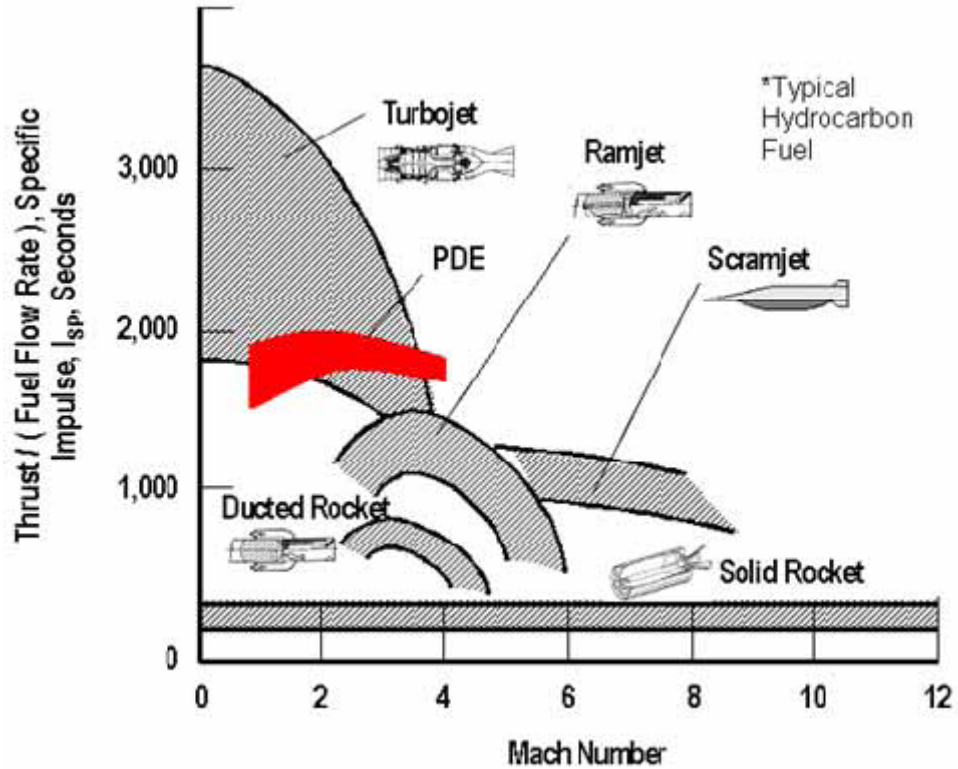
Figure 1.   Comparison of High-speed Propulsion Technologies (From [1]).

Figure 1 reveals that turbojet engines exhibit superior performance at Mach numbers below Mach 3, since above this value the complexity of the required advanced materials needed for these turbines minimizes the advantages of these propulsion systems. Above Mach 3, Ramjet and scramjet engines approach the performance level of turbojet engines. These engines do not have the ability to operate at low Mach numbers since the inlet air is compressed by the diffuser, which requires a booster to attain the initial flight speed necessary for engine start.

Detonation-based propulsion systems, such as PDEs, have a greater operating range covering the subsonic region through high Mach numbers. The PDE combines high performance, efficiency, and simplicity thus making it a viable mode of propulsion for tactical missile applications. Other concepts incorporating detonation-based propulsion are a hybrid PDE gas turbine system and a combined cycle PDE for single stage to orbit launch vehicles.

In order to capitalize on the benefits of detonation-based propulsion, efficient initiation of the detonation in a short distance is critical. However, using obstacles to initiate detonation can result in total pressure losses, which results in a loss of efficiency. Comprehending the initiation mechanisms for detonation will allow designs that are more efficient and also maximize the frequency of repeatability. This research examines the initiation mechanisms through experimental observations and computer simulations for several obstacle configurations that are known to produce detonations in order to generate guidelines for the use of specific obstacle configuration.

THIS PAGE INTENTIONALLY LEFT BLANK

II. BACKGROUND

A. COMBUSTION PROCESSES

Detonation is one of the three primary modes of combustion. It is different from the other modes of combustion based on the speed of propagation, the shock wave created, and the effects of this shock on the continuing process. A detonation event can be produced almost instantaneously from several options such as the use of an explosive charge, high energy ignition, or shock focusing if sufficient conditions exist. A conventional burning process can also be manipulated to transform into a detonation.

1. Deflagration

The most common form of combustion is deflagration. This method can be approximated by a constant-pressure combustion process; this form of combustion takes place in turbojet engines and also closely approximates diesel engines. In a perfect deflagration event, a combustion wave propagates through the mixture at subsonic speeds, with combustion and the resulting energy release occurring only at the flame front and leaving combustion products in its wake without a pressure rise. A more realistic model is that the deflagration wave speed is limited due to physical limitations that keep the velocities subsonic. The temperature, pressure, and structure of the advancing flame front have a robust affect on the chemical reaction rates of the substances involved. The chemical reaction rates govern the energy release rate that will further limit the flame speed, since combustion can only occur when the flame front makes contact with the reactants. Introducing turbulence into the event will increase the total flame area and subsequently increase the rate of consumption of the reactants. Deflagration results in a relatively large release of entropy, resulting in lower thermodynamic efficiencies [2].

2. Detonation

Detonation occurs when a supersonic shock wave propagates through a reactive mixture and compresses it, which results in a prompt increase in temperature, pressure,

density, thus intensifying the reaction rate. An extremely energetic mixture develops directly behind the shock wave and promptly combusts in a violent, exothermic reaction that supports the previous shock wave and the two become dependent on each other. The compression and coupling properties in a detonation event result in a much larger enthalpy gain than from a deflagration event.

3.   Deflagration versus Detonation

Comparing the attributes between deflagration and detonation emphasizes the differences between the two. A one-dimensional (1D) model of a combustion wave is shown in Figure 2 and reveals the basic properties of a combustion process. In the combustion wave reference frame, unburned reactants with velocity u_1 are located to the left of the stationary combustion wave and burned reactants with velocity u_2 are to the right.
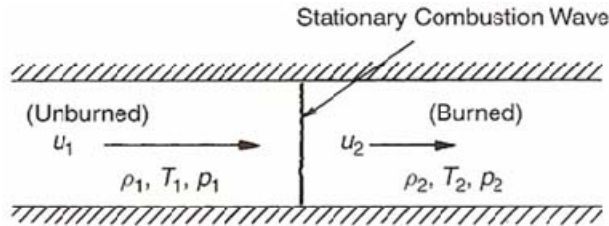
Figure 2.   Stationary One-Dimensional Combustion Wave Model (From [2]).

Based on Figure 2, Table 1 lists the differences between deflagration and detonation for velocity (u), density (ρ), temperature (T), and pressure (p) before and after the combustion wave. When compared with deflagration, the difference in pressure and temperature following the detonation wave are significant; this difference and the lower overall increase in entropy make detonation much more efficient than other types of combustion.

Table 1.   Comparison of Detonation and Deflagration Characteristics (From [2]).

	Detonation	Deflagration
u_1/c_1	5-10	0.0001-0.03
u_2/u_1	0.4-0.7 (deceleration)	4-16
p_2/p_1	13-55 (compression)	0.98-0.976 (slight expansion)
T_2/T_1	8-21 (heat addition)	4-16 (heat addition)
ρ_2/ρ_1	1.4-2.6	0.06-0.25

B.   DETONATION THERMODYNAMICS

In order to understand the purpose of this research, a review of thermodynamics and detonations is necessary. The simple one-dimensional model of Figure 2 can be characterized thermodynamically through the Hugoniot curve. The assumptions applied to this elementary model include the perfect gas law as well as the conservation of mass, momentum, and energy.

Perfect Gas Law: $$p = \rho RT \tag{1}$$

Conservation of Mass: $$\rho_1 u_1 = \rho_2 u_2 \tag{2}$$

Conservation of Momentum: $$p_1 + \rho_1 u_1^2 = p_2 + \rho_2 u_2^2 \tag{3}$$

Conservation of Energy: $$c_p T_1 + \frac{1}{2}u_1^2 + q = c_p T_2 + \frac{1}{2}u_2^2 \tag{4}$$

where q is the specific heat added to the system and c_p is the specific heat at constant pressure, equivalent to:

$$c_p = \frac{\gamma}{\gamma - 1}R \tag{5}$$

Where gamma is the ratio of specific heats:

$$\gamma = \frac{c_p}{c_v} \tag{6}$$

For a constant area problem, Equation (2) illustrates that mass flow rate ($\dot{m}$) must be constant and when combined with Equation (3) yields the Raleigh-Line relation. The slope of the Raleigh-Line indicates the velocity of the detonation wave.

Raleigh-Line Relation:
$$\rho_1 u_1^2 = \frac{p_2 - p_1}{\dfrac{1}{\rho_1} - \dfrac{1}{\rho_2}} = \dot{m} \tag{7}$$

The Hugoniot Relation may be obtained by manipulating the Raleigh-Line relation of Equation (6) through substitution of Equations (1), (3), (4), and (5) and solving for q; this yields a form that cancels the velocity conditions u1 and u2, relating the heat release per unit mass.

Hugoniot Relation:
$$\frac{\gamma}{\gamma-1}\left(\frac{p_2}{\rho_2} - \frac{p_1}{\rho_1}\right) - \frac{1}{2}(p_2 - p_1)\left(\frac{1}{\rho_1} + \frac{1}{\rho_2}\right) = q \tag{8}$$

Equation (8) describes the Hugoniot Curve of Figure 3, which, for any combustion mixture with a given q and initial conditions p_1, ρ_1, displays all mathematically possible combinations of p_2 and $1/\rho_2$.
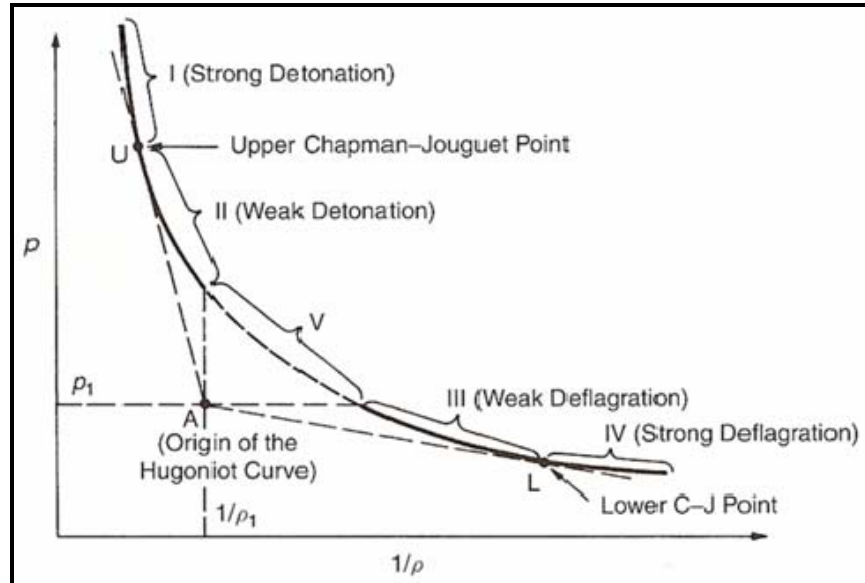
Figure 3.   Hugoniot Curve Divided by Theoretical Regions (From [2]).

Figure 3 states that there are five possible regions on the Hugoniot curve, each one a theoretical combustion condition. These five regions are created by a constant pressure line, a constant specific volume line, and tangent lines drawn from the origin of the curve defined by the initial conditions p_1 and ρ_1 (labeled point A on Figure 3). The tangent lines intersect the curve at the upper and lower Chapman-Jouguet (C-J) points, U and L. All of the regions, while mathematically possible, are not observed; Region V is physically impossible as it requires $p_2 > p_1$ and $1/\rho_2 > 1/\rho_1$, which would result in an imaginary velocity for u_1 in Equation (7).

Regions I and II are transient in nature. Region I is considered the strong detonation region since $p_2 > p_u$, and requires an overdriven shock. Region II is called the weak detonation region and requires exceptionally fast chemical reactions. Region IV is the strong deflagration region and is not a possible steady-state solution. Therefore, the only possible regions for steady state solutions are Region III, weak deflagration and the Upper C-J point, U, the solution point for detonations [2].

The velocity of the burned reactants can be found by differentiating and re-arranging the Hugoniot Relation, resulting in the slope of the curve, Equation (9):

Slope of the Hugoniot Curve:
$$\frac{dp_2}{d(1/\rho_2)} = \frac{(p_2 - p_1) - \left(\frac{2\gamma}{\gamma-1}\right)p_2}{\left(\frac{2\gamma}{\gamma-1}\right)\frac{1}{\rho_2} - \left(\frac{1}{\rho_1} + \frac{1}{\rho_2}\right)} \quad (9)$$

And equating it with the slope at the C-J points, Equation (9):

Slope at C-J Points:
$$\frac{dp_2}{d(1/\rho_2)} = \frac{p_2 - p_1}{1/\rho_2 - 1/\rho_1} = V_{\text{det}} \quad (10)$$

Finally combined with the Rayleigh-Line Relation of Equation (7):

Velocity at C-J Points:
$$u_2^2 = \frac{\gamma p_2}{\rho_2} = c_2^2 \quad (11)$$

9

Both detonation and deflagration results in the burned reactants moving at a velocity equal to the local speed of sound and away from the wave. Directly behind the shockwave is a reaction zone that is characterized by subsonic flow, which allows the chemistry

C.   DETONATION STRUCTURE

After the formation of a detonation wave, the event is maintained due to the strong coupling of the detonation shock wave and the combustion event that occurs just behind the shock wave. Zeldovich, von Neumann, and Döring developed this theory first for detonation and created a one-dimensional model that demonstrates this event [2]. Figure 4 is a ZND model representing a one-dimensional detonation wave.
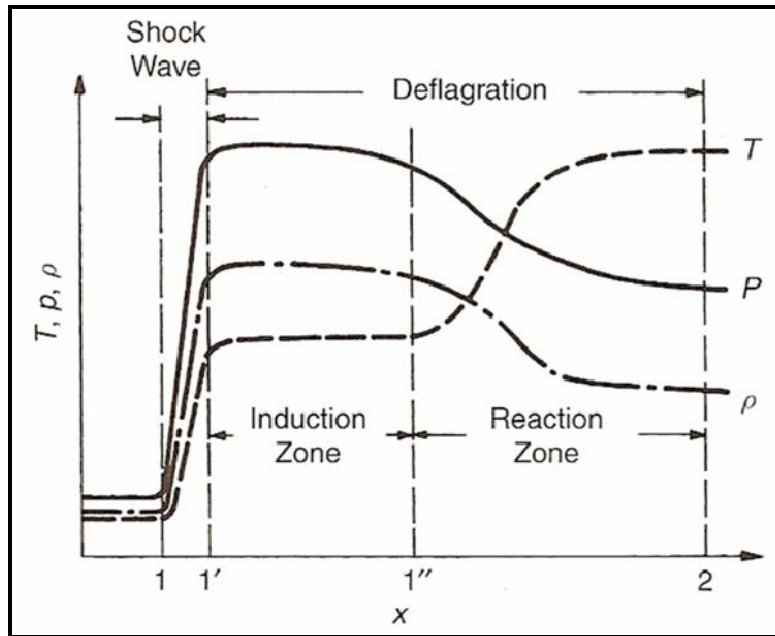
Figure 4.   ZND Detonation Wave Profile (From [2]).

This ZND model consists of a leading supersonic shock wave, which causes a rapid increase in temperature and pressure in the reactants. After the shock wave is an induction zone; this reaction is traveling at subsonic velocities thus allowing the chemistry to support the initial shock by creating further sonic disturbances. A highly energetic and efficient chemical reaction takes place in the reaction zone, which sustains the shock wave.

The one-dimensional model is sufficient for explaining the critical characteristics of a detonation but the actual event is much more complex and is shown in Figure 5. Figure 5 uses a soot foil technique that is able to image the shock waves. The leading shock wave is actually comprised of many small, divergent shock waves that are followed by perpendicular shocks interacting with each other as well as the leading shock wave. These shock wave interactions form triple points, which are visible in Figure 5.

Figure 5.   Image of Three-Dimension Nature of a Detonation Wave (From [2]).

D.   THERMODYNAMIC ADVANTAGES OF DETONATIONS

The useful energy lost in a thermodynamic process corresponds to an increase in entropy(s); the lower the rise in entropy due to combustion, the more energy available that can be extracted into useful work, thus a more thermodynamically efficient process. Relative to other combustion processes, detonation shows evidence of a very high thermodynamic efficiency.

Figure 6 shows the relative values of entropy for the different regions of the Hugoniot curve of Figure 3. From Figure 6, it can be seen that the Lower C-J point corresponds to the maximum value of entropy which is described as strong deflagration. The minimum entropy value happens at the Upper C-J point, where detonation is the dominant process. Based on this observed difference in entropy for the various methods of combustion, detonation is the most efficient combustion process [2].
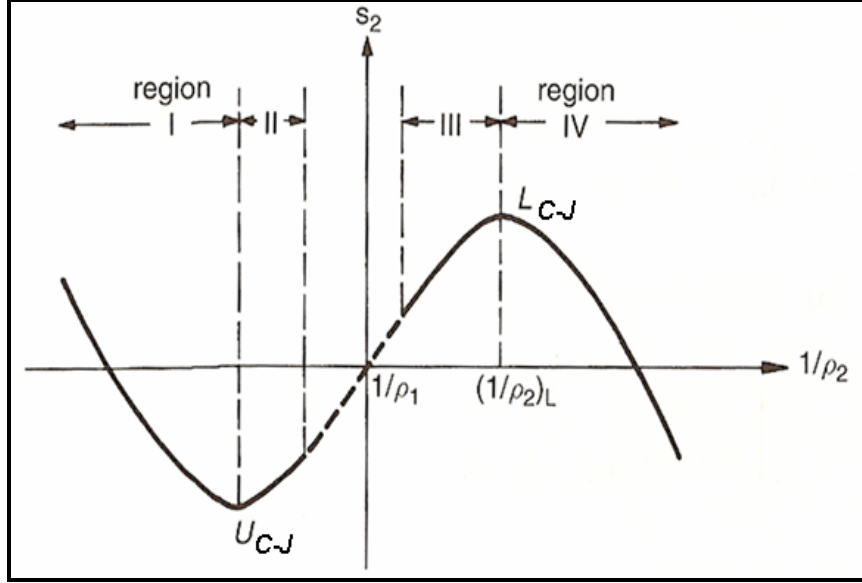
Figure 6. Entropy Distribution on the Hugoniot Curve (From [2]).

E. DEFLAGRATION-TO-DETONATION TRANSITION

Detonation can be created by several initiation methods. Some of these methods include high-energy ignition, shock focusing, explosive charges or deflagration-to-detonation transition (DDT) [2]. In order for detonation to become a viable option for propulsion, the detonation event must be repeatable and at a high enough frequency in which an effective amount of thrust is created. Initiating the detonation using DDT does not limit the frequency of repeatability and is also a relatively simple approach.

Initially the deflagration process is started by a reactive mixture igniting and forming a small kernel of combustion. The resulting flame front then expands as it moves down the combustor and produces pressure waves ahead of the flame front. Ultimately, the multiple compression waves will combine into a single shock wave which results in the flame front breaking up due to the turbulence. Breaking up of the flame front causes an increase of the flame surface area thus increasing the reaction rates and energy release until an "explosion within an explosion" occurs in the reaction zone (Figure 7). Two resulting shock waves result: the super-detonation wave traveling forward into the unburned gases and a retonation wave moving toward the rear of the combustor. In addition to these shock waves, a spherical shock wave develops as well as transverse

12

waves created from the oscillations between the two larger shock waves (Figure 8). A final steady detonation wave is created by the interactions of these shock waves as they travel down the combustor [2].
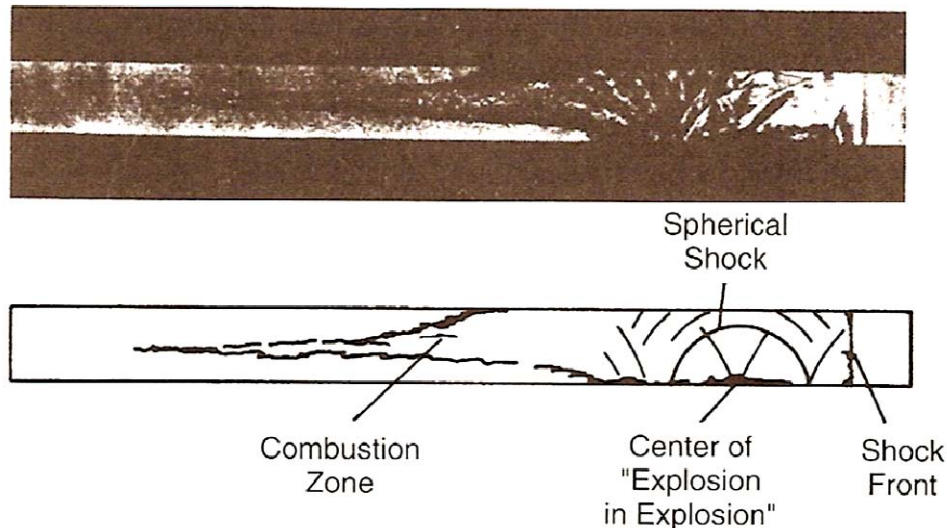
Figure 7.   DDT "Explosion within an Explosion" (From [2]).
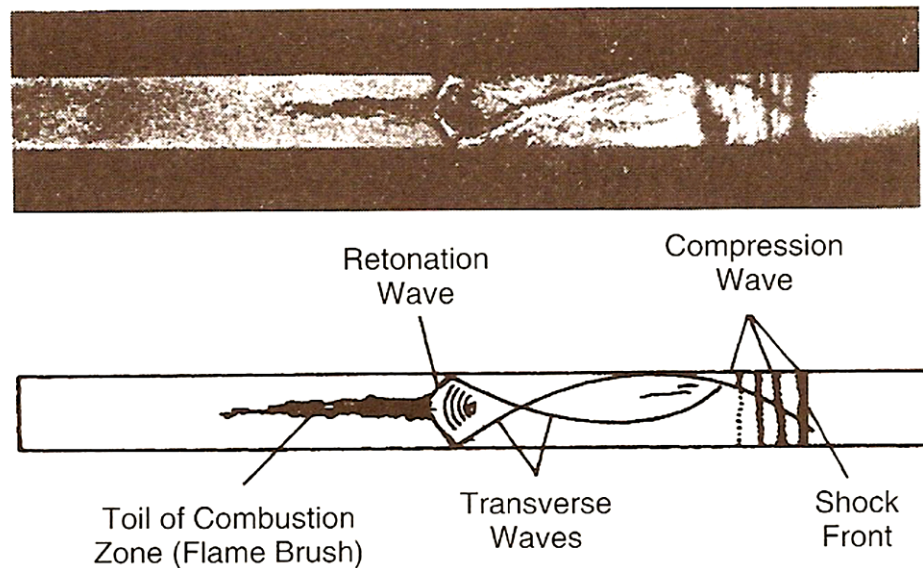
Figure 8.   DDT transverse Waves (From [2]).

Wall effects and the autoturbulization which results in high-intensity turbulence can cause the transition to detonation as long as the tube is of sufficient length. This autoturbulization causes additional wrinkling of the flame, which increases the flame surface area and leads to detonation.

In order to shorten the distance required for DDT, turbulence can be intentionally created by placing obstacles in the flow field as shown in Figure 9. Obstacles in the flow field assist in the formation of shock-focused "hot spots" that lead to self-ignition of the fuel ahead of the flame front which results in the acceleration of the reaction zone. Together these phenomena considerably raise the reaction rates, which result in an increased compression wave strength. Obstacles currently being evaluated for their benefits include ramps, screens, tabs, and Shchelkin spirals.

Weak ignition and slow flame propagation

Flame folding and onset of turbulence

Obstacles

Turbulent flame acceleration and shock formation

Onset of detonation

DDT or run-up distance

Propagation of detonation
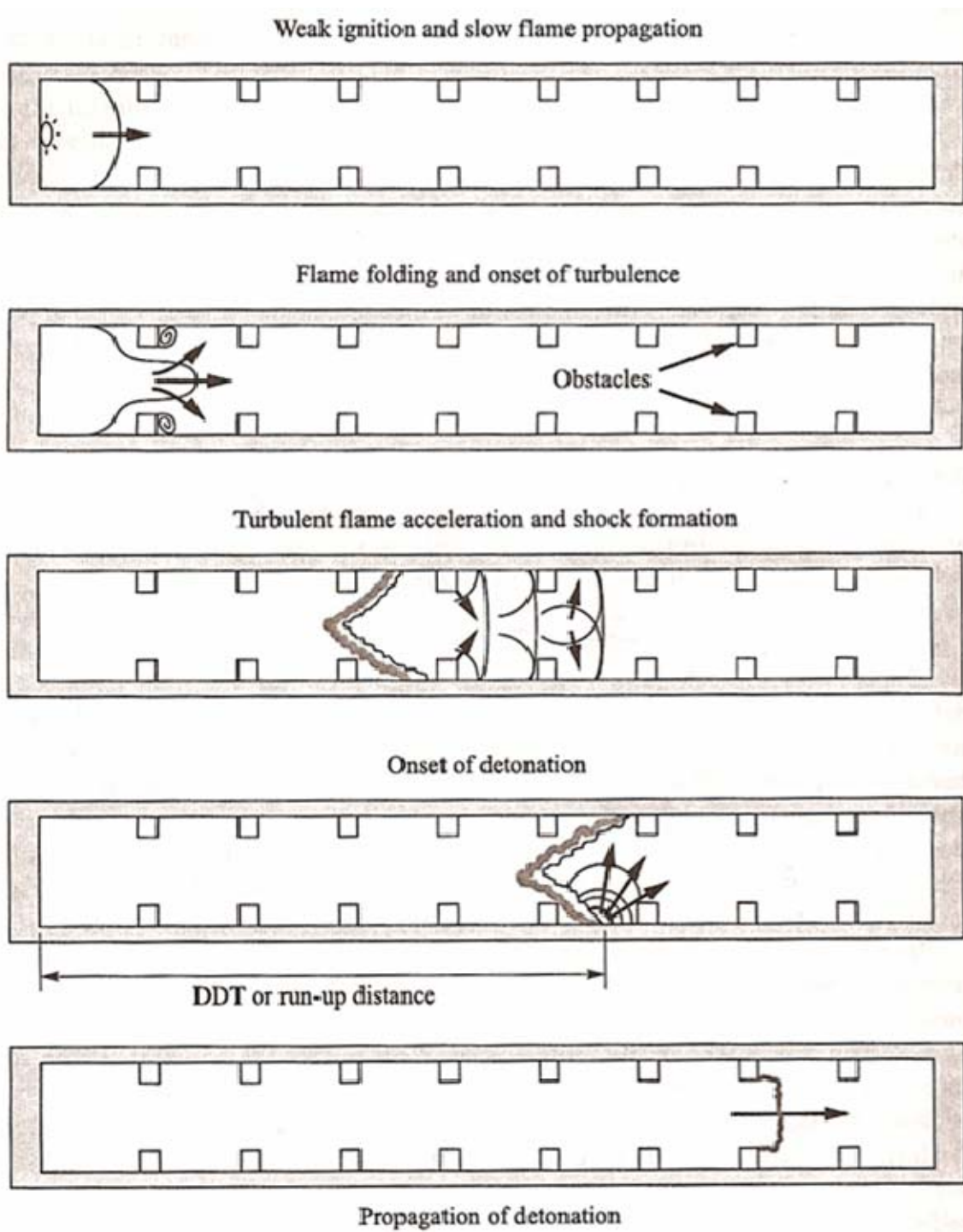
Figure 9.   Sequence of DDT Acceleration in Tube with Obstacles (From [3]).

15

F.   PULSE DETONATION ENGINES.

In order to produce thrust sufficient for propulsion, the detonation events must occur at a high enough frequency. This concept forms the basis of operation of the pulse detonation engine. Figure 10 demonstrates a single cycle of a simplified standard pulse detonation engine. This model assumes that a valve gas delivery system is used to direct reactants during the appropriate time.

1. Reactants injected	5. Detonation wave exits
2. Tube fills	6. Rarefaction waves
3. Mixture ignited	7. Products exhausted
4. Detonation wave forms	8. Cycle repeats
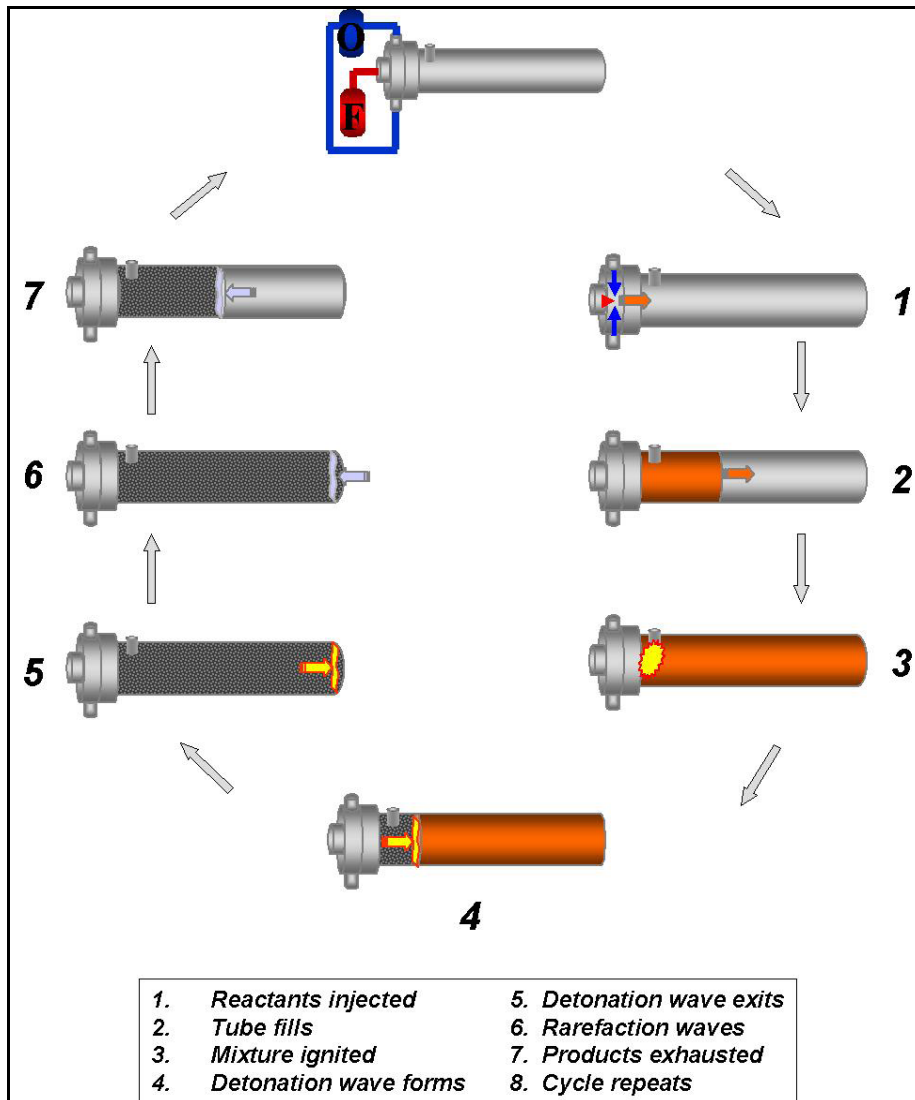
Figure 10.   Ideal PDE Operation Cycle (From [4]).

Thrust is generated only during the detonation phases of this cycle; in order to produce a near-constant thrust, the overall cycle time must be held to a minimum. The

fill, blow-down, and purge cycle times are all extremely reliant on the length of the chamber. The obstacles that are used to enhance DDT can have a negative impact on the process by increasing the pressure loss through the combustor. Therefore, the ideal design for a PDE is one that minimizes the pressure losses from obstacles and the ignition delay due to filling requirements.

THIS PAGE INTENTIONALLY LEFT BLANK

III.   DESIGN/EXPERIMENTAL SETUP

The experimental testing was conducted at the Naval Postgraduate School, Rocket Propulsion Laboratory, Test Cell #1. The test apparatus was comprised of a combustor section, shock formation tube, test section, optical viewing section, and exhaust tube (Figure 11). Gaseous ethylene (C_2H_4) and air ($O_2 + 3.76\ N_2$) were used as reactants and were pre-mixed prior to injection into the combustion section. The ignition of the ethylene/air mixture was initiated by a high capacitance igniter mounted in the head flange of the combustion section. The instrumentation used during testing included high-speed pressure data acquisition integrated with a high-speed digital camera that captured the images in the optical test section. The entire test assembly was supported by a Newport Research Corporation optical table. The actuation and instrumentation for the test cell was accomplished remotely in the control room via a National Instruments GUI. Operation of the camera was also controlled from the control room but from a separate computer.
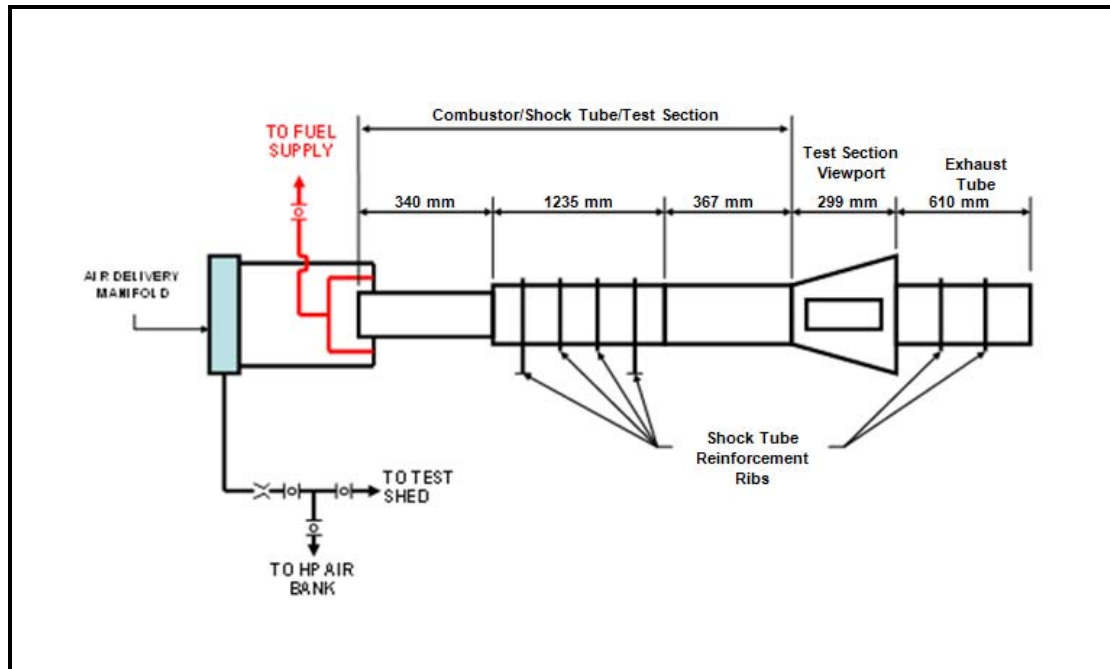
Figure 11.   Diagram of the Experimental Assembly.
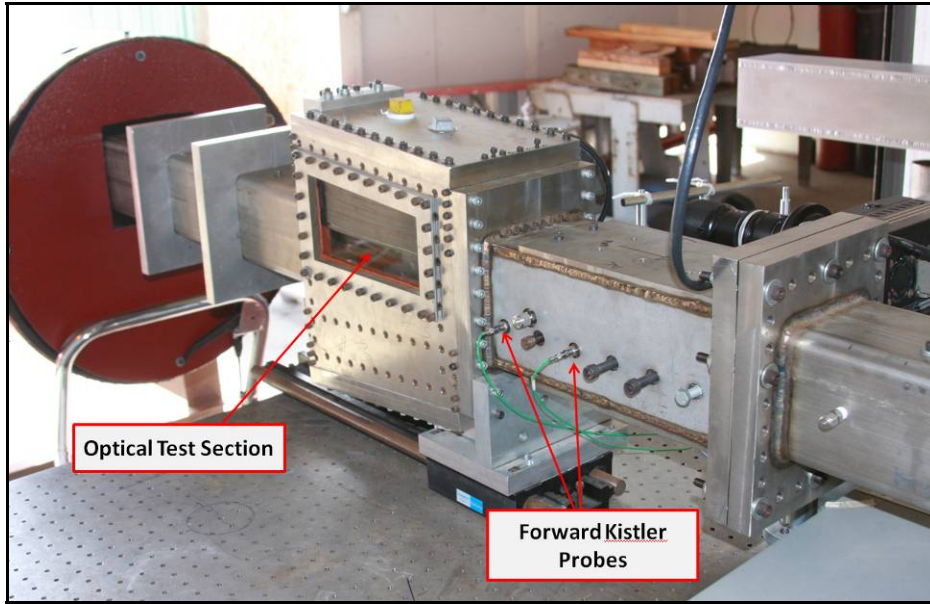
Figure 12.　　　　Test Cell #1 Experimental Setup.

A.　DESCRIPTION OF THE EXPERIMENTAL ASSEMBLY

1.　Combustor

The purpose of the combustor section was to generate a fully developed deflagration wave and the associated shock.　The combustor section was made of a 112.71 mm diameter stainless steel tube 340 mm in length (Figure 13).　The inlet for the air/fuel mixture was located 25.4 mm from the combustor head and entered through two 25.4 mm diameter tubes welded to the steel tube 180 degrees apart.　Located on the head of the combustor was an igniter flange for the high capacitance igniter and it was shielded by a cone shaped shroud as shown in Figure 14.　The purpose of the shroud was to protect the nascent flame from being extinguished during high flow rate testing. Attached to the downstream end of the combustion section is the shock formation tube.
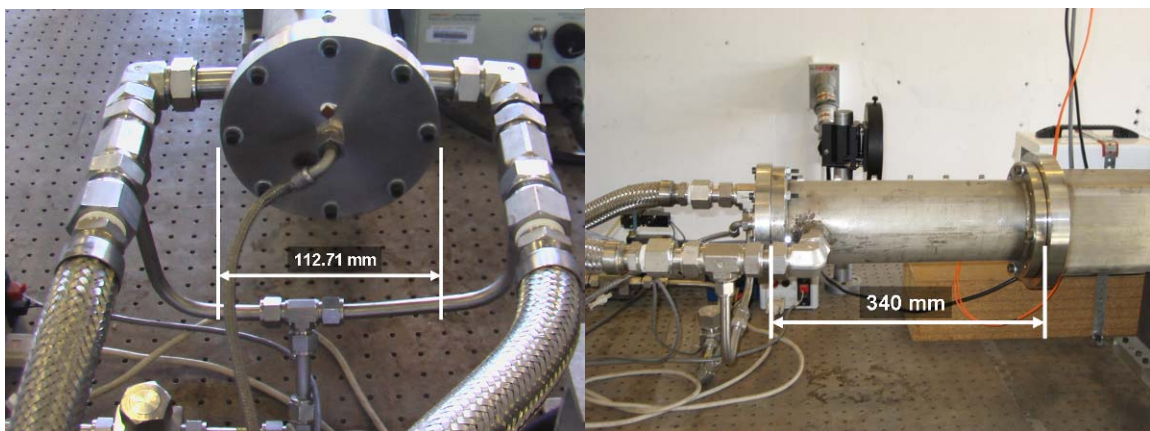
Figure 13.   Forward and Side View of the Combustion Section.
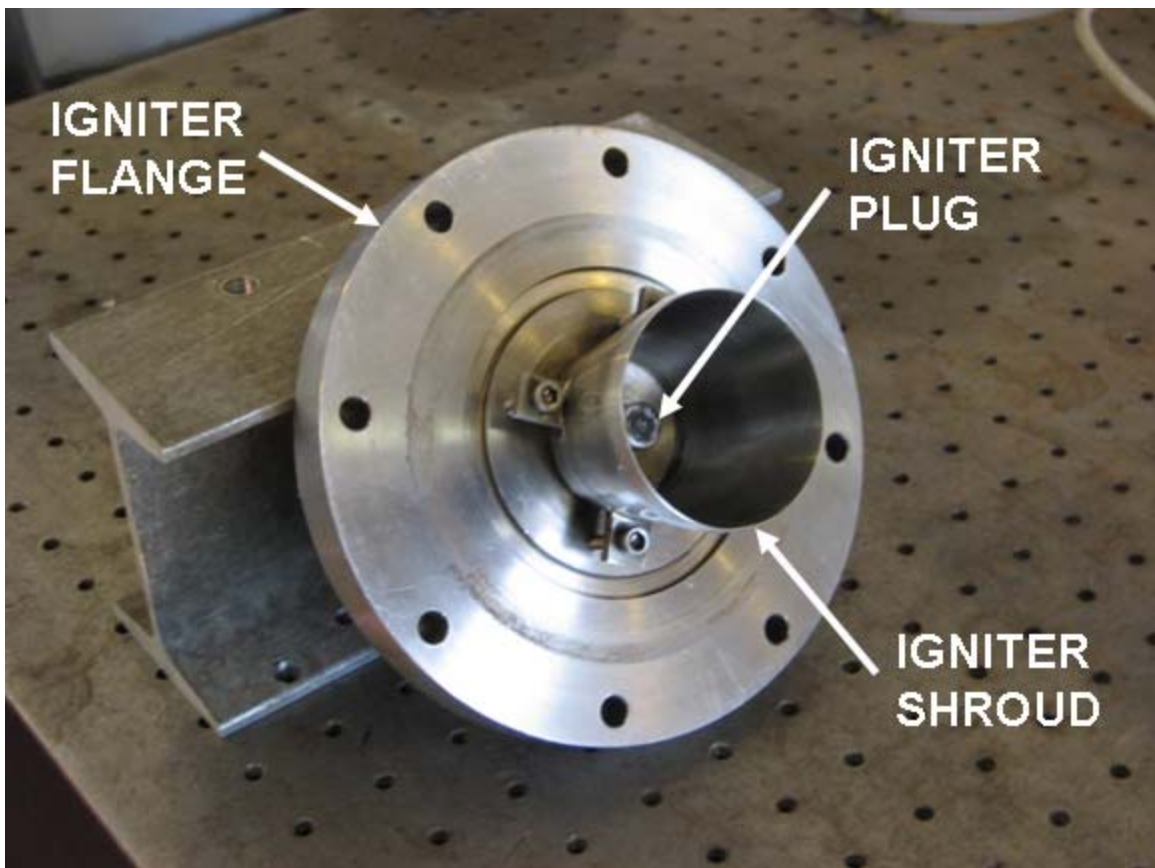
Figure 14.   View of Igniter Flange with Shroud and Igniter Installed.

21

2. Shock Formation Tube

In order for the combustion shock to become fully developed and separated from the combustion wave, a shock formation tube of sufficient length was necessary. The shock formation tube enabled the formation of a combustion-driven normal shock wave prior to entering the test section. The shock formation tube was a 123.5 cm long, 13.0 cm square stainless steel tube. Michael A. Fludovich constructed this section for use in earlier thesis work [5]. To prevent deformation of this section during testing, four ribs made from 2.54 cm aluminum plate spaced along the shock formation tube. The test section was fastened to the aft end of the shock tube via fasteners and an o-ring seal.

3. Test Section

After the shock formation section was the test section which was also designed by Fludovich to allow a smooth transition from the larger 13.0 square shock formation tube to the 114 mm x 80 mm test section [5]. The test section was designed with several types of connections to allow various instrumentations. During this testing, two high-speed Kistler pressure transducers spaced approximately 10 cm axially along the centerline were installed as shown in Figure 15. High-speed Kistler pressure transducers were used to determine shock speed entering the test section. An optical sensor that was able to detect the flame front passage was also installed in this section, providing a trigger signal to the high-speed camera as shown in Figure 15.
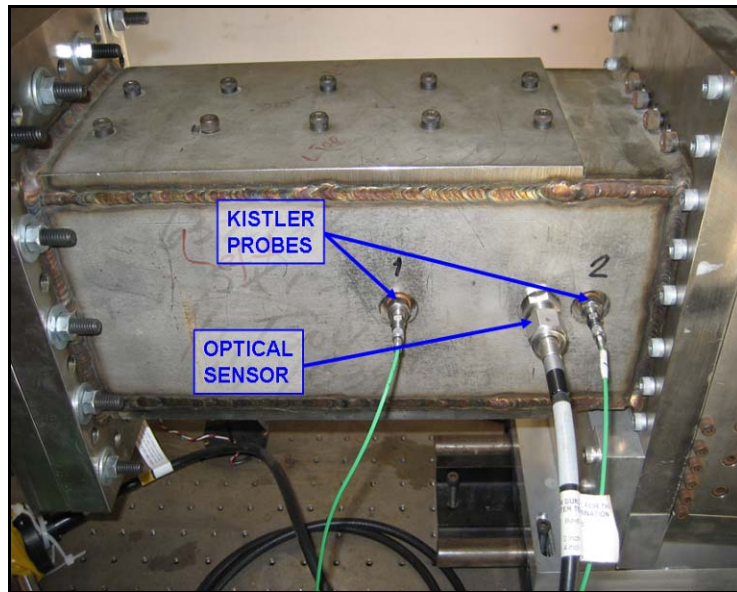
Figure 15.   Test Section Detail Showing Kistler Probes and the Optical Sensor.
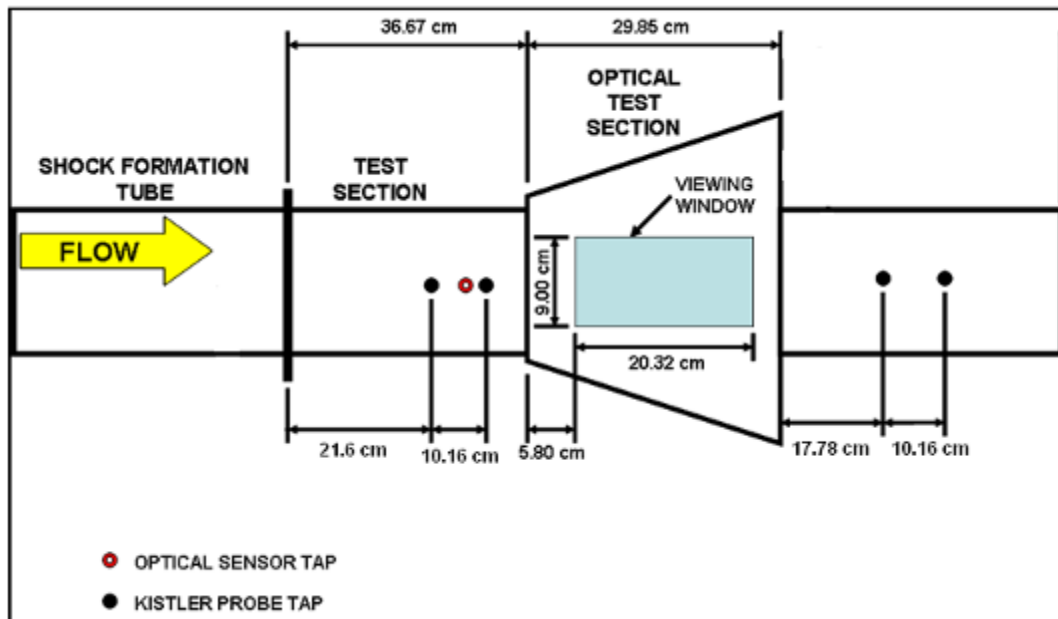
Figure 16.   Test Section Drawing with Dimensions.

4.   Optical Test Section

The optical test section was a previous nozzle inlet that was designed by Fludovich [5]. The nozzle inlet had been modified since the nozzle components had been removed and replaced with plates extending from the test section. The two windows in

the optical viewing section were 30.48 mm thick and were mounted flush with the sections walls, forming an imaging area 9 cm x 20.32 cm (Figure 16). The aft end of the optical test section had mounting brackets for attachment of the exhaust tube section. To facilitate additional testing, one of the windows was removed and replaced with an aluminum insert of the same dimensions. This aluminum insert allowed swept ramps to be mounted centerline on the vertical wall. This configuration allowed the existing imaging equipment to catch a top-down perspective of the detonation event as it occurred behind the obstacles.

5. Ramp Mounting Plates

Two ramp mounting plates were designed to allow mounting of the swept ramps both on the top and bottom of the test assembly. The mounting plates were 137.8 cm x 8 cm and were tapered at the front end as shown in Figure 17. The two ramp mounting plates were mounted to the top and bottom of the test assembly via fasteners. The ramp mounting plates were mounted in four sections of the assembly: the shock formation tube section, test section, optical test section, and the exhaust tube. Both of the plates were constructed with an array of tapped holes which permitted multiple ramp configurations to be tested. The fastening holes were plugged when not in use to prevent any of the combustion products from filtering through the plate during testing. The same swept-ramp obstacles as used by Anderson [7] were used in this thesis. The details of the ramp geometry are given in Appendix A. With both ramp mounting plates installed, the resulting area for the optical test section was 76.2 mm x 114 mm (Figure 18).
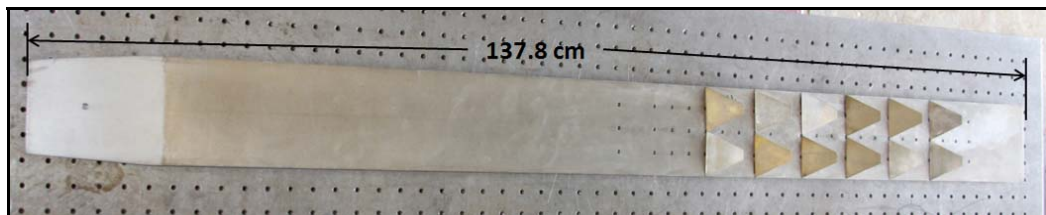
Figure 17.   Swept Ramp Removable Mounting Plate with 6 Rows of 2 Ramps.

Figure 18.   End View of Combustor with Exhaust Tube Removed.

6.   Exhaust Tube

A removable exhaust tube was installed downstream of the optical test section to isolate the test section from ambient flow disturbances and also direct the shock and combustion products away from the test table and instrumentation (Figure 19).   The exhaust section was a square tube which had two Kistler pressure transducers mounted centerline 10.16 cm apart along the right side of the exhaust tube.   These sensors provided precise measurements of the shock speed after the test section which allowed a comparison to the upstream shock velocity measurement.   The exhaust tube was inserted into the test cell exhaust tube, which minimized the pressure waves that could be directed back toward the instrumentation and cameras during testing.
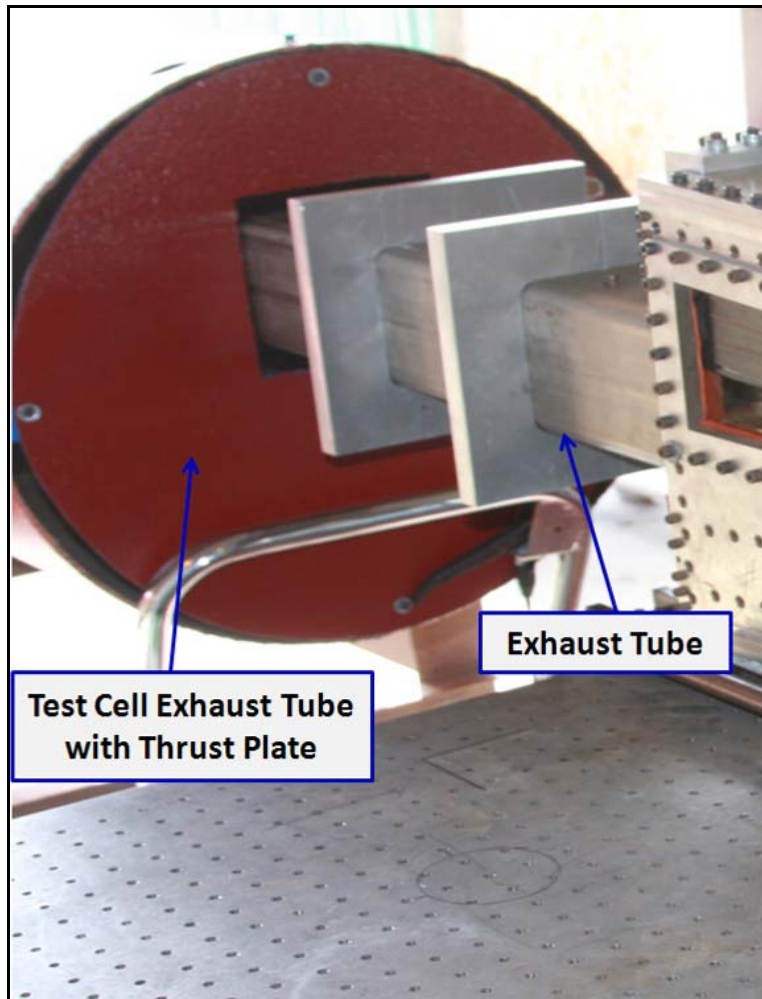
Figure 19.   Exhaust Tube and Test Cell Exhaust Tube.

B.   AIR AND FUEL DELIVERY

High pressure (HP) air was provided to the test cell from the facility air system and ethylene was provided from a single bottle.   The main control room computer controlled the supply pressures for both HP air and ethylene with the Tescom ER3000 Version 2.0 software; this allowed the pressures of the reactants to be set remotely and independently of each other (Figure 20).
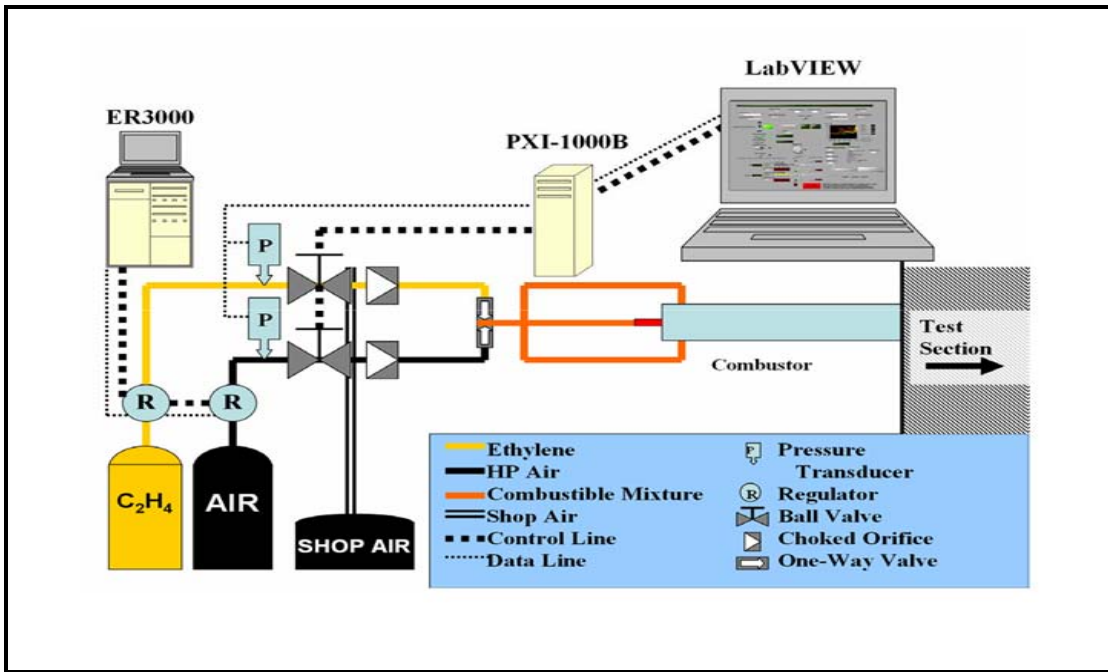
Figure 20.   Schematic Diagram of Air and Fuel Delivery System (From [8]).

Air was supplied through 1½-inch piping that was connected to a single inlet manifold and from there routed to the combustion section via flexible steel hoses. Ethylene gas was supplied via ½-inch tubing that was connected to each of the air inlets prior to entering the test section; these are shown in Figure 21.
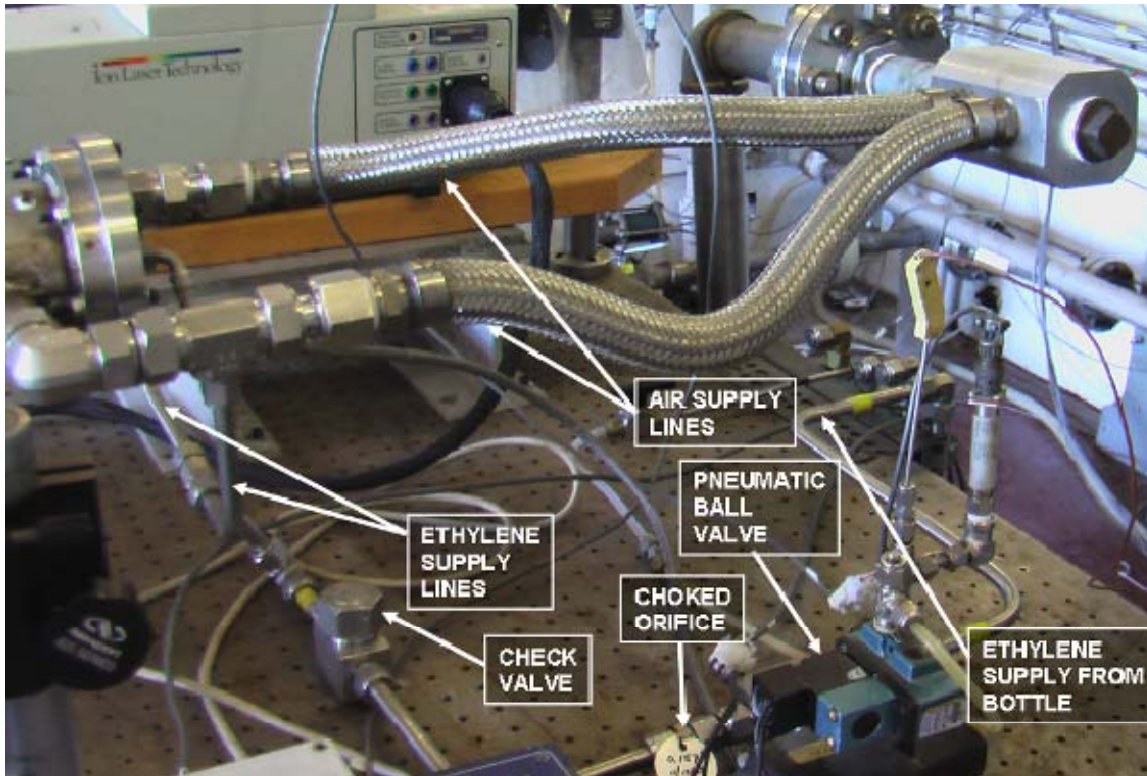
Figure 21.   Fuel and Air Supply Delivery System.

Air flow was initiated by the using the ER3000 regulator controller. Ethylene was injected into the combustor through a single Swagelock ball valve that was opened at the desired time for the desired time length. This ball valve was air actuated and controlled by the LabVIEW software via Crydom control solenoid switches located in an electronics cabinet located in the test cell (Figure 22).
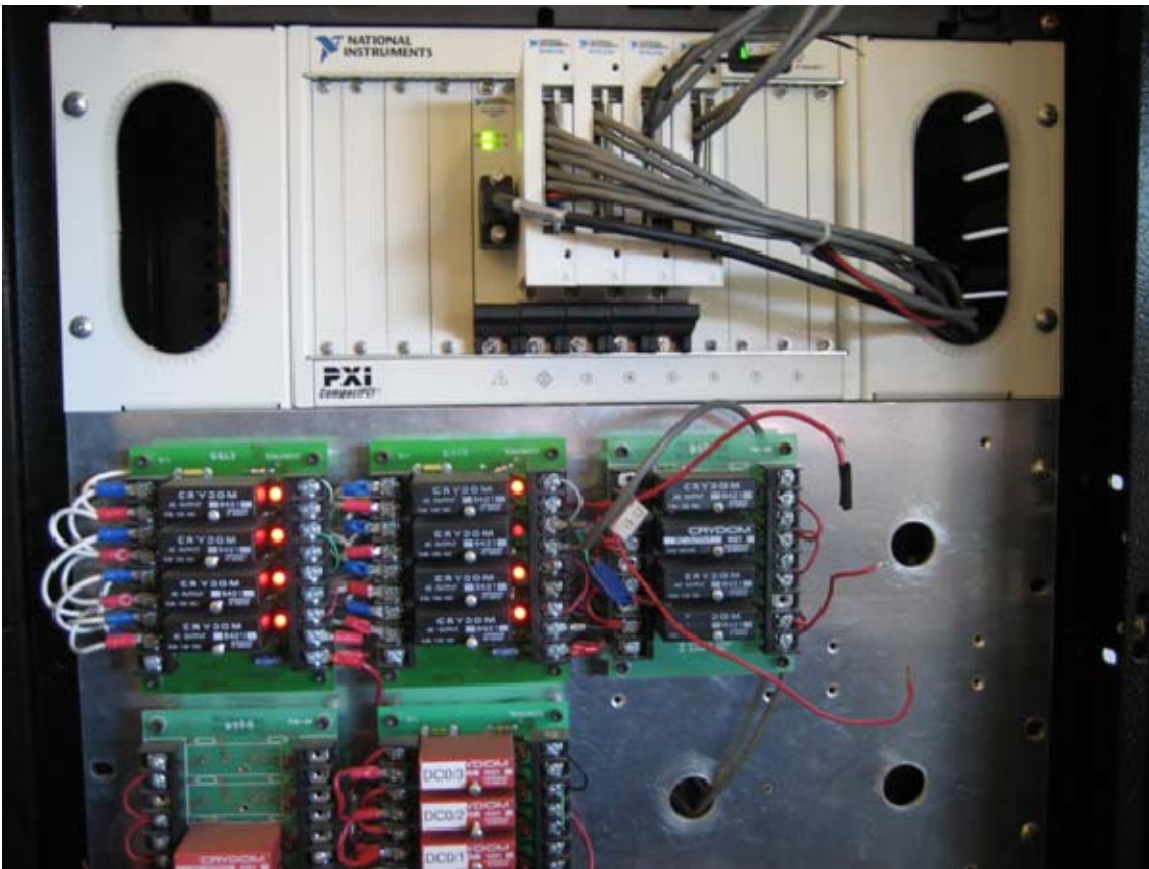
Figure 22.   PXI-1000B Chassis (Upper Section) and Crydom Control Solenoid Switches (Lower Section).

An orifice was located in both of the supply lines to provide an accurate method of controlling the mass flow rates for each gas. The choke diameters used during this testing were 0.236 inches for the air supply and 0.157 inches for the ethylene supply. A check valve located between the combustor and the ball valve was installed to prevent the possibility of backflow due to the combustion event (Figure 21).

C.   IGNITION SYSTEM

The ignition system used in this test assembly was the Unison Vision-50 Variable Ignition System and is shown in Figure 23. This ignition system is a capacitive discharge type system that uses an aviation grade spark plug mounted in the head of the combustor section. Prior to testing the igniter was configured manually to provide a 2 Joule spark and was remotely triggered by the LabVIEW software.

Figure 23.   Unison Ignition System.

D.   INSTRUMENTATION

The instrumentation used during testing controlled the initiation as well as data collection. Each of the four pressure signals were routed through one of four National Instruments (NI) 14-bit PXI-6115 cards mounted in the NI PXI-1000B chassis, shown in the upper half of Figure 22. This chassis interfaced with the computers in the control room through the NI PXI-MXI-4 PXI Bridge and was capable of collecting either real time or high-speed buffered data. Optical data imaged from the high-speed camera was routed to a dedicated desktop computer in the control room using a fiber optic line. A schematic of the data acquisition system is shown in Figure 24.
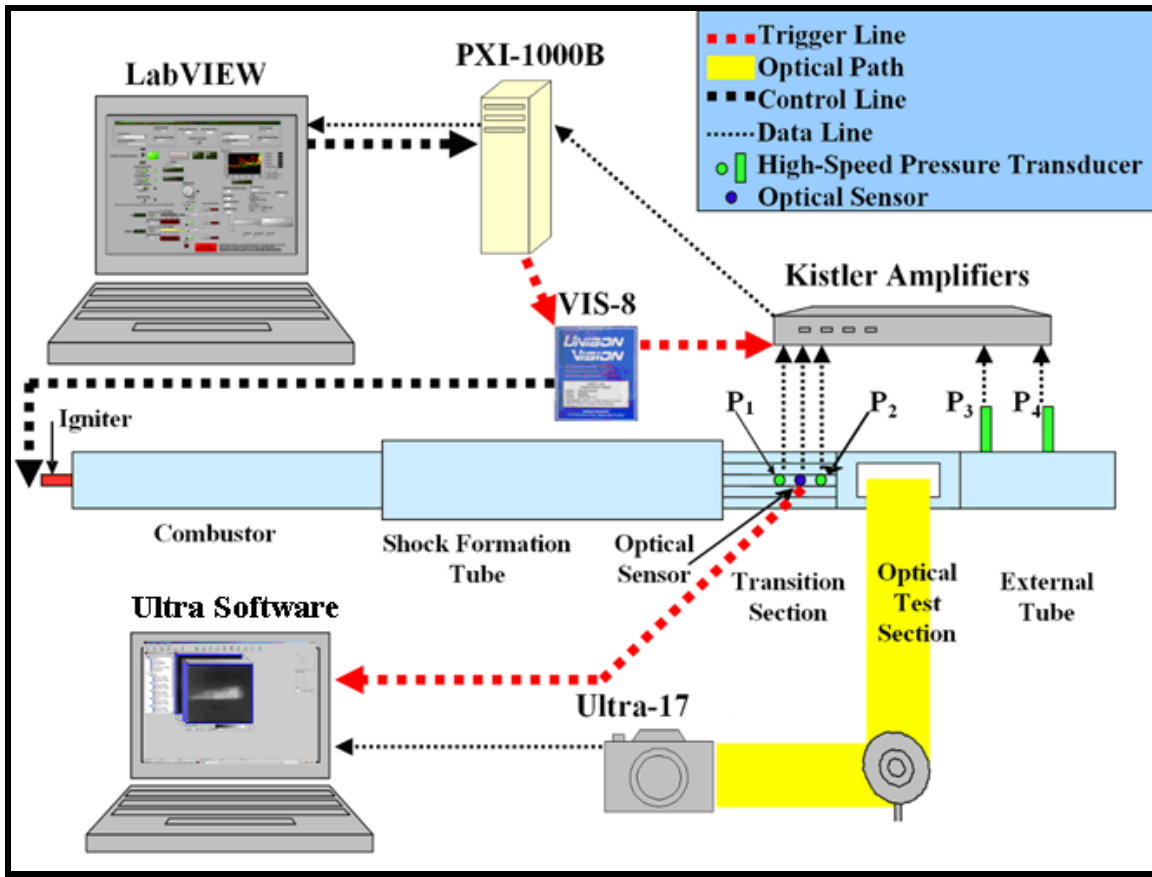
Figure 24.   Schematic of Ignition and Instrumentation (From [7]).

1.   Dynamic Pressure Transducers

Before and after the test section were four high-frequency Kistler dynamic pressure transducers mounted in pairs in order to calculate the wave velocity based on the pressure transients. The pressure transducers were connected to Kistler Type 5010 Dual Mode amplifiers which then routed the data to two NI PXI-6115 data cards in the PXI-1000B for high-speed data collection. Once the testing sequence was initiated, the cards were configured to begin collecting data with the triggering of the capacitive discharge igniter and collected data at a rate of 500 kHz. The data was stored in the card buffer and was later saved to the computer located in the control room. The pressure data supplied by the Kistler transducers provided high resolution of shock passage.

2. Optical Sensor

An optical sensor was inserted in the test section, 13.8 cm prior to the optical test section, and was used to activate the imaging equipment once it detected the passage of the flame front. With the flame detected, the optical sensor triggered the camera to begin collection of high-speed flame images.

3. Ultra 17 High-Speed Imaging System

An Intensified Ultra 17 CCD camera from DRS Data & Imaging Systems, Inc. was used to image the optical test section. The Ultra 17 was able to image and store up to 17 high-speed frames per test run with a resolution of 512 x 512 pixels per frame with a 12 bit dynamic range. The Ultra 17 was equipped with an image intensifier which had the ability to provide a gain of up to 15,000 times in 100 discrete steps. The system was capable of imaging up to 157,000 frames per second [9].

The Ultra 17 camera was controlled from the control room with a dedicated computer using a Hotlink fiber optic connection. Images from the test section were reflected off a mirror to the camera that was aligned parallel to the combustion tube as shown in Figure 25. The camera was triggered remotely from the signal generated from the optical sensor. A Nikon ED AF NIKKOR 80-200 mm 1:2.8 telephoto lens was attached to the camera allowing focused image of the optical test section (Figure 26).
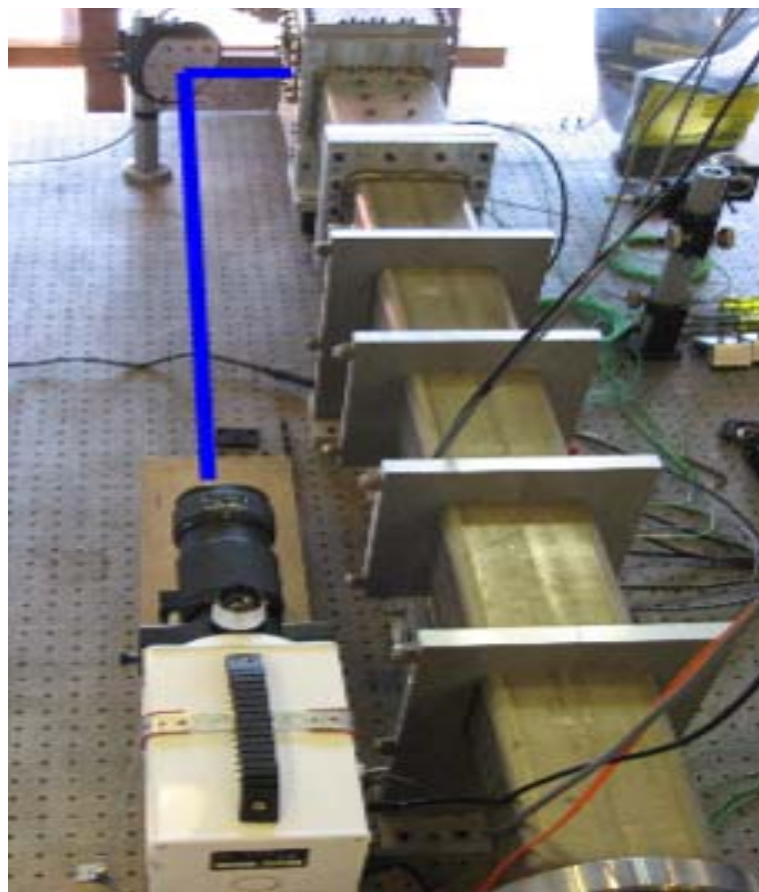
Figure 25.   Photo and Diagram Illustrating Camera Setup for Flame Imagery.

Figure 26.   Intensified Ultra 17 CCD High-speed Camera.

The Ultra computer program allowed the camera to be configured and armed remotely. The images were transferred to the control room computer running the Ultra software where the images were cataloged and stored.

4. Princeton Instruments Camera

Another camera utilized was a Princeton Instruments camera. The camera utilizes a charge-coupling device (CCD) array. This camera was triggered by an external optical sensor which then used a programmable gate pulse generator to input the appropriate delay. Mounted to the lens of the camera was a filter that allowed wavelengths of 425 nm to 435 nm to pass through. This wavelength correlates to chemiluminescence from the Carbon Hydrogen radicals (CH*) during a combustion event.

5. Shimadzu Hyper-Vision 2 High-Speed Camera

Approximately three quarters through testing the Ultra 17 malfunctioned and DRS Data & Imaging Systems loaned the lab a replacement. The replacement camera was a Shimadzu Hyper-Vision 2 high-speed camera (Figure 27). The camera was to image up to one million frames a second and store 99 frames. The camera speed was set to 125 kfps allowing a 4 μsec exposure time. A Nikon ED AF NIKKOR 80-200 mm 1:2.8 telephoto lens was attached to the camera allowing focused image of the optical test section. The camera was triggered remotely from the signal generated from the optical sensor.

Figure 27.   Shimadzu Hyper-vision 2 High-speed Camera.

E.   SOFTWARE DESCRIPTION AND FUNCTIONS

The software used during this experimental testing included Cequel, LabVIEW, and Ultra (Figure 28).   These programs offered the ability to control all of the test instrumentation and equipment, but also provided the analysis tools. All applications were run on desktop PCs using Microsoft Windows.

1.   CEQUEL

The chemical reaction characteristics were calculated using the CEQUEL Toolbox: Chemical Equilibrium in Excel Version 1.75 from Software and Engineering Associates, Inc. / Spreadsheet World, Inc. The CEQUEL plug-in was installed for use with Microsoft Excel 2003 and determined the theoretical combustion products and characteristics of different compounds for multiple reactions.

The required inlet mass flow rates of air and ethylene supplied to the test section were determined from the desired equivalence ratio (φ). The equivalence ratio relates the fuel/oxidizer ratio of a given mixture to the ideal stoichiometric ratio of the mixture and is defined by Equation (12):

$$\phi = \frac{\dot{m}_f / \dot{m}_o}{\left[\dot{m}_f / \dot{m}_o \right]_{stoichiometric}}$$

(12)

35

The stoichiometric ratio is a theoretical chemical reaction where complete combustion has taken place; therefore, no reactants remain after the event. In an actual combustion event, complete combustion will never occur since dissociation is always present. Another factor that prevents complete combustion is that complete mixing of the reactants does not occur, thus preventing the reactants in the mixture to react completely. The stoichiometric equation for an ethylene (C_2H_4) and air ($O_2+3.76N_2$) is shown in Equation (2):

$$C_2H_4 + 3(O_2 + 3.76N_2) \rightarrow 2CO_2 + 2H_2O + 3(3.76N_2)$$

(13)
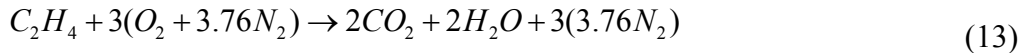
When a fuel/air ratio is fuel rich, unreacted fuel constituents will remain after combustion; this condition occurs when the value of the equivalence ratio (φ) is greater than one. When the equivalence ratio is less than one, the fuel/air ratio is fuel lean and unreacted oxygen remains after combustion. Regardless of the value of φ, nitrogen is present but is considered a non-reactive component.

CEQUEL calculated the mass flow rates required to produce equivalence ratios ranging from 0.8 to 1.6. Inlet supply pressures for air and ethylene were determined by assuming a constant supply temperature for the choke diameters installed in each of the supply lines using the isentropic flow relationship of Equation (14) [10]:

Choked Mass Flow Rate:
$$\dot{m} = \left(\frac{A_2 p_t}{\sqrt{T_t}} \right) \Gamma_2 K_\Gamma$$

(14)

where:
$$K_\Gamma = \sqrt{\left[\left(\frac{g_c}{R} \right) \left(\frac{2\gamma}{\gamma-1} \right) \left(\frac{2}{\gamma+1} \right)^{\frac{2}{\gamma-1}} \left(\frac{\gamma-1}{\gamma+1} \right) \right]}$$

(15)

and $K_\Gamma = 1$ (choked flow).

The air and ethylene pressures inputted into the ER3000 were calculated from Equation (14) with the mass flow rates previously determined from CEQUEL.

36

2. LabVIEW

Actual testing was controlled remotely from the control room with LabVIEW Professional Development System Version 8.5 and a graphical Virtual Interface (VI) developed specifically for the experiment (Figure 28) installed on a desktop PC. When the LabVIEW software and the VI were placed in the run mode, the VI controlled the injection of fuel, igniter initiation, and collection/archiving of the test data.
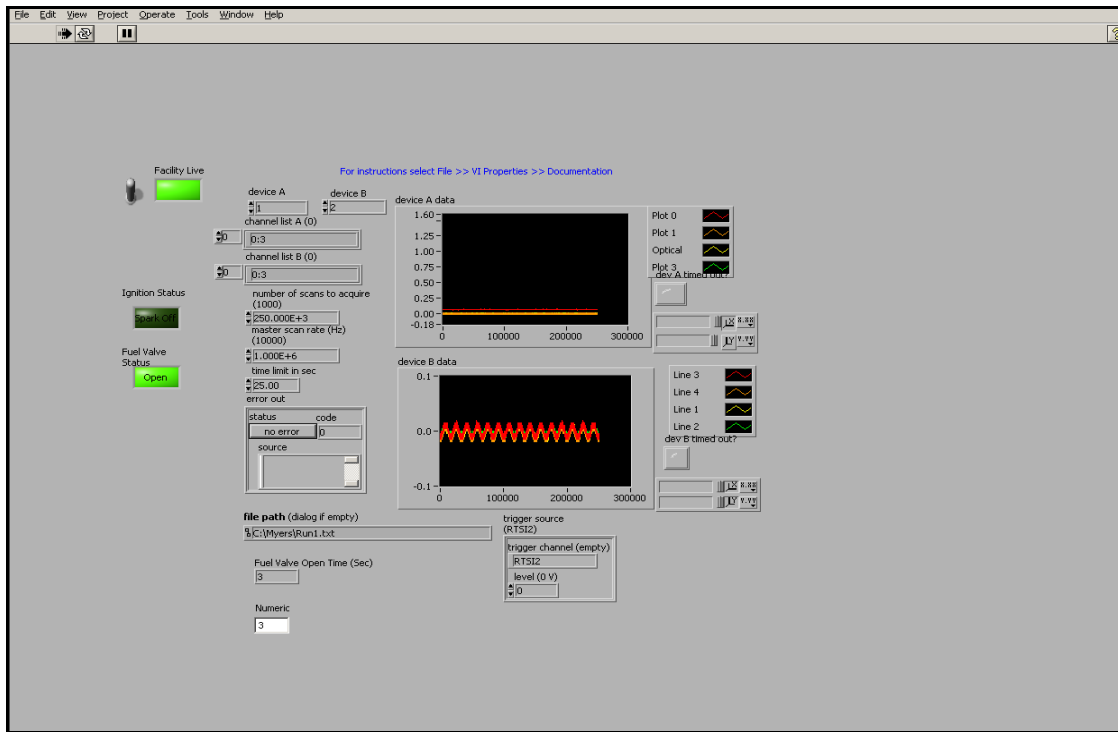
Figure 28.   Screen Capture of LABVIEW VI Used During Testing.

3. Ultra 17 Camera and Ultra Software

The Ultra 17 high-speed camera was controlled from a dedicated desktop PC in the control room executing the Ultra Software, Version 1.1.19.1. The Ultra software is a Windows-based program issued by DRS Data & Imaging Systems, Inc. The software was used to program the imaging sequence as well as to arm the camera. Once armed the camera was triggered by a signal from the optical sensor located in the test section.

THIS PAGE INTENTIONALLY LEFT BLANK

IV. EXPERIMENTAL RESULTS

A. PURPOSE

The purpose of this testing was to observe the conditions before, during and after the detonation event. Various devices were used to record the actual event. The data recorded from the high-speed pressure transducers determined if a detonation occurred. The sequence of events surrounding a detonation event were recorded, analyzed and then compared to the results derived from the computer simulations in order to study the mechanisms responsible for the initiation of detonation.

B. OBSTACLE FREE TESTING

Initially testing was conducted with all obstacles removed from the test assembly in order to verify the set-up and operation of the imaging and data collection procedure. Multiple tests were conducted at various conditions to verify the test equipment was properly installed. The data recorded during all test included the pressure transducer values, fuel pressure, air pressure, the optical sensor output, and the images of the event. High-speed Kistler pressure transducers were used to record the pressure waves (shocks) produced by the combustion event due to the initial shock wave and then the actual combustion wave (Figure 29).
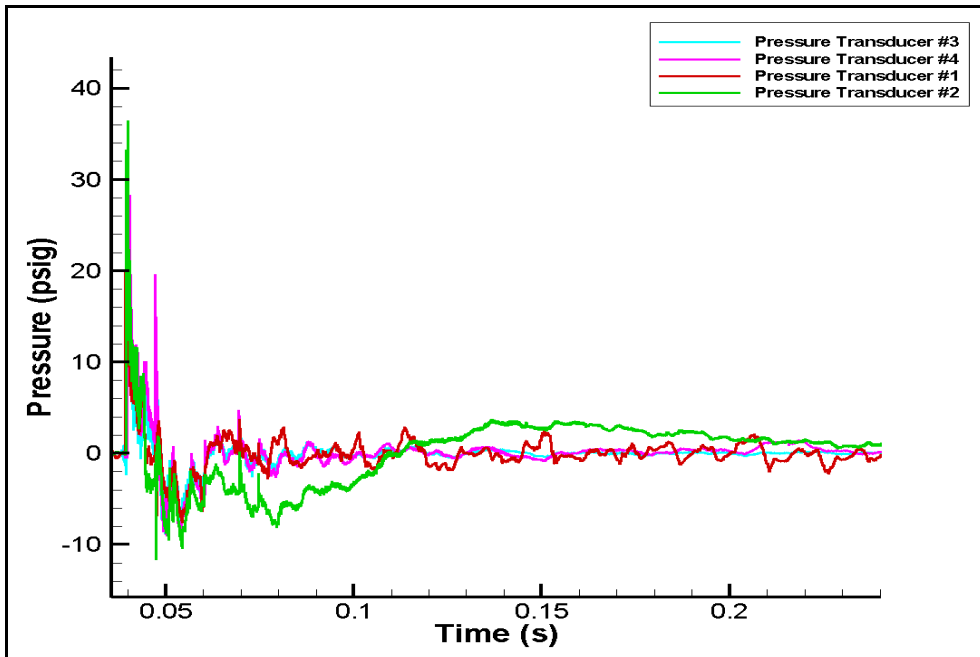
Figure 29.   High- Speed Pressure Traces for Obstacle Free Configuration.

The combustor fill rate for this test had a characteristic Mach number value of 0.1 with the fuel/air mixture at an equivalence ratio (φ) of 1.4. The pressure transducers 1 and 2 recorded an initial pressure spike at 39.3 and 39.4 milliseconds, respectively, caused by the passing of the initial shock created by the combustion event (Figure 30). Knowing the distance between the probes and this time difference, a shock speed of 558.3 m/s was calculated. The initial shock continued toward the exit of the assembly and registered on the pressure transducers 3 and 4 at 39.6 and 39.8 m/s respectively, which corresponded to a velocity of 561.3 m/s. The actual combustion wave follows the shock wave by approximately 0.75 milliseconds, which causes the second pressure spike in pressure transducers 1 and 2 at 39.95 and 40 milliseconds. The data recorded during the obstacle free testing reveals that the initial edge of the combustion wave follows the trailing edge of the initial shock wave by approximately 200 µsec.
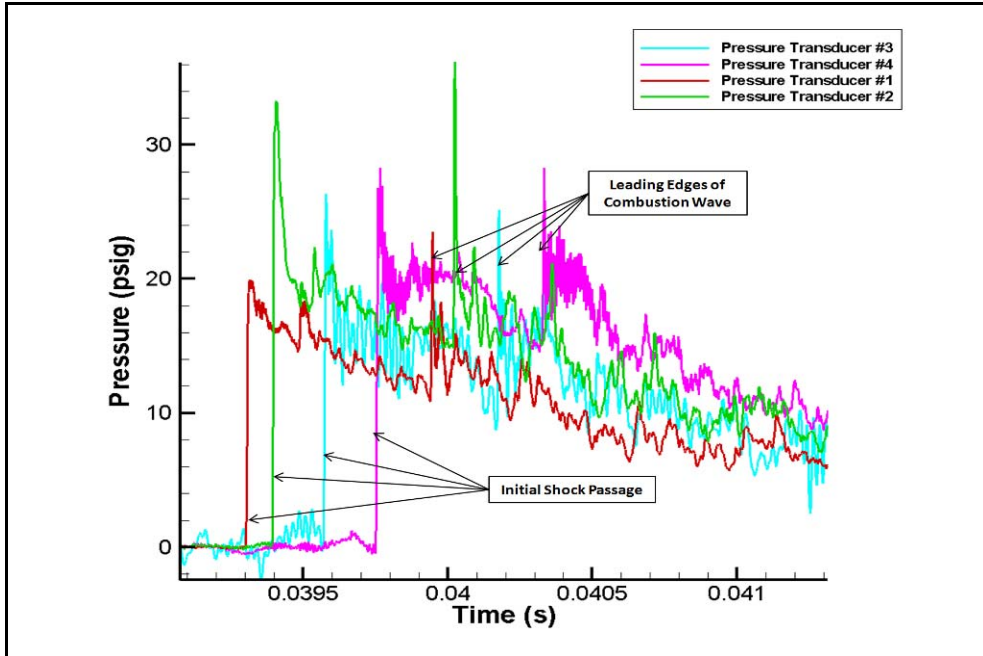
Figure 30.   Pressure Traces of Figure 29 Magnified to Show Event Edges

This approach to calculate the combustion and shock wave velocities were used in later tests with obstacles to initially determine if a detonation event occurred.

C.   SWEPT RAMP TESTING

Two swept ramp configurations were tested. These arrangements were selected based on the success of previous testing conducted [7]. The first obstacle arrangement consisted of various rows of ramps located along the centerline of the ramp mounting plate and a mirrored ramp located on the opposing ramp mounting plate. The second configuration tested consisted of multiple rows consisting of 2 ramps mounted side by side. The testing for these arrangements consisted of 5 and 6 rows of ramps with φ ranging between 1.0 and 1.7.
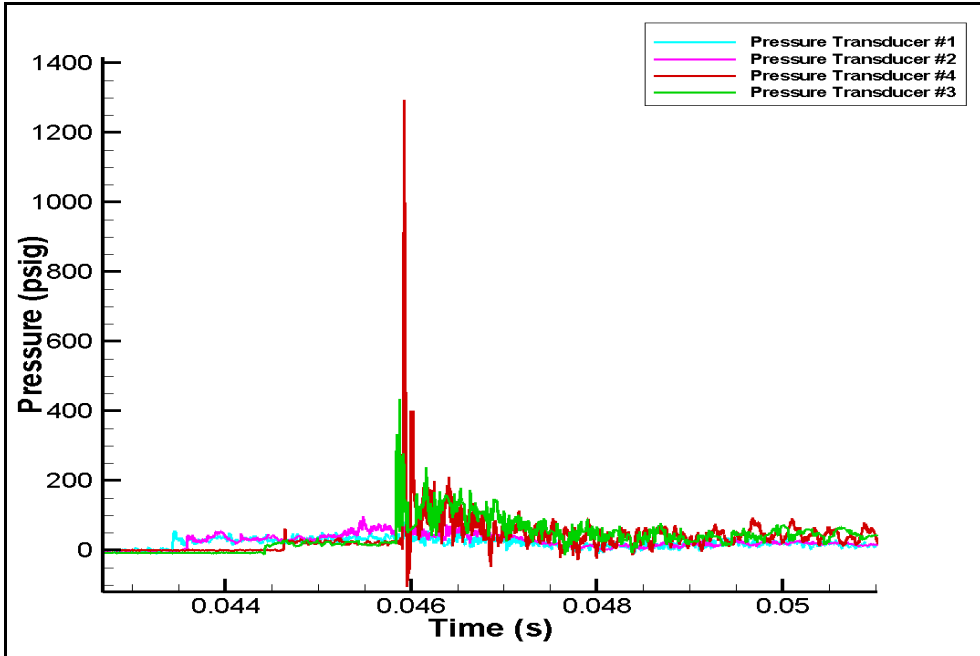
Figure 31.   High-Speed Pressure Traces for a 5 Rows of Centerline/Opposing Ramps.

Figure 31 is the high-speed trace illustrating detonation in combustor for 5 rows of ramps mounted centerline and opposing. Pressure transducer #4 registered pressures in excess of 1300 psi. The combustor fill rate for this test had a characteristic Mach number value of 0.1 with the fuel/air mixture at an equivalence ratio (φ) of 1.23 and a shock speed of 2309 m/s. These measurements reveal that an over-driven detonation occurred. An over-driven detonation event is not a steady state condition but is a transient event since the detonation event will move downward along the Hugoniot curve (Figure 3) towards the Upper C-J point, where it becomes a stable detonation event.

D.   HIGH-SPEED IMAGERY

1.   Side View of Flame Imagery

Once detonations were verified from the shock wave velocities, high-speed imaging was used to analyze the flame front interactions in order to better understand the initiation of detonations. Figure 32 shows selected frames of a detonation event. These images are from the same test that produced the high-speed traces of Figure 31.

42
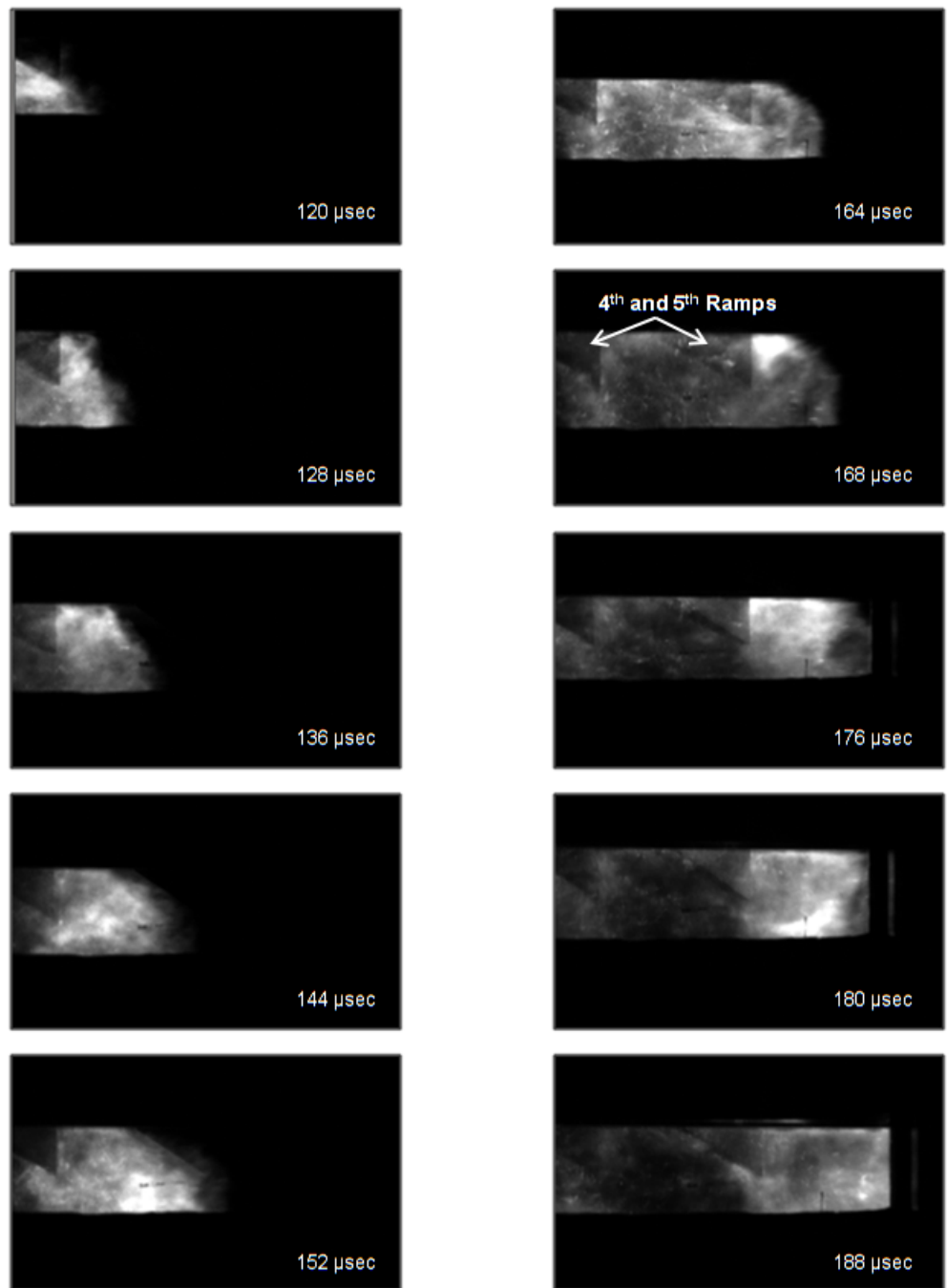
Figure 32.   High-speed Imagery of Flame Front Interactions 5 Swept Ramps Located
Centerline and Opposing.

From Figure 32, bright illuminations were visible behind the 4th and 5th swept ramps as can be seen at 136 µsec and 168 µsec. These illuminations were located approximately 0.57 step heights behind the ramp (Figure 33). These illuminations appeared to be responsible for the detonation initiation observed shortly thereafter.
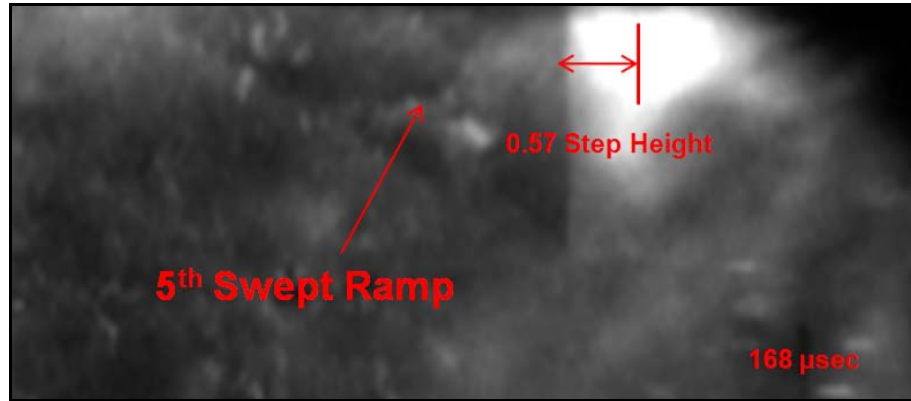
Figure 33.   Illumination Step Height.

2.   Top-Down View of Flame Imagery

In order to determine if the detonations were occurring along the centerline of the ramps, imaging of the detonation from a top-down perspective were needed. To facilitate the additional imaging, one of the windows from the optical test section was removed and replaced with an aluminum insert of the same dimensions. This aluminum insert allowed swept ramps to be mounted centerline on the vertical sidewall opposite from the camera. This configuration allowed the existing imaging equipment to view a top-down perspective of the detonation event as it occurred behind the obstacles. The bottom edge of the optical window bisected the vertical ramps equally thus only the top half of the swept ramps was visible.

To ensure detonation was achieved, 5 rows of 2 ramps were mounted upstream on one of the ramp mounting plates. Three additional ramps were then mounted to the vertical sidewall. With this configuration, a fuel/air mixture ($\varphi=1.27$) was ignited and detonation verified by wavespeed calculation. At time 108 µsec and 132 µsec, bright illuminations were present along the centerline and directly behind the 2nd and 3rd vertically mounted ramps (Figure 34).
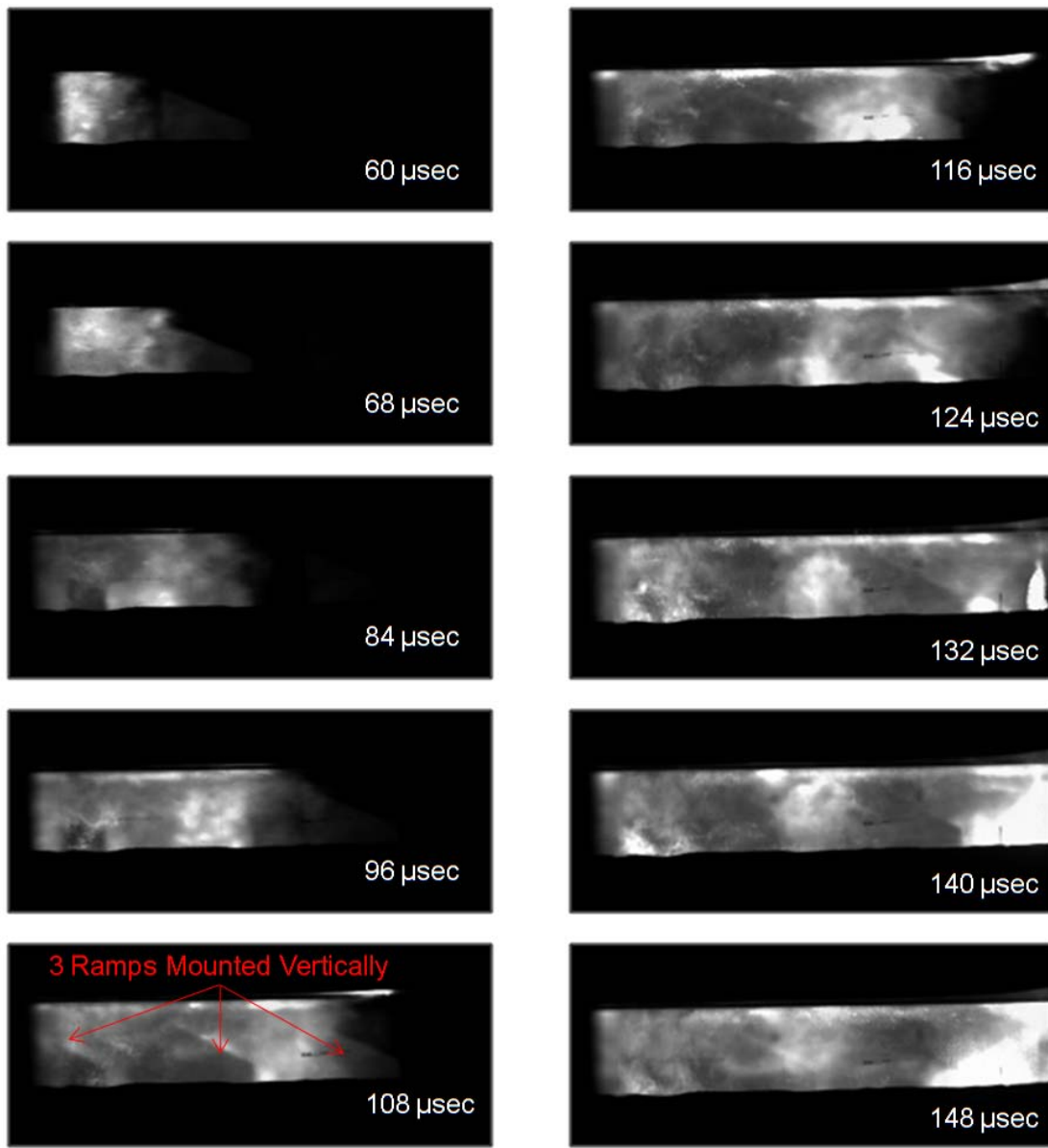
Figure 34.   Top-down View of Flame Interacting with Obstacles

3.   CH* Imaging

The bright illuminations visible behind the obstacles could have been caused by several scenarios, such as compression of the gases or a combustion event. In order to validate that these sites were due to the onset of detonation, additional evidence was needed. Another camera equipped with a filter was utilized in order to compare filtered versus unfiltered images. A Princeton Instruments camera was triggered from the same

optical sensor and imaged a single frame. Knowing the delay programmed into the Princeton Instrument's camera, the same point in time was imaged from two different cameras and analyzed. Mounted to the lens of the Princeton Instrument's camera was a filter that allowed wavelengths of 425−400 nm to pass through. This wavelength correlates to CH chemiluminescence from a combustion event and is an excellent marker for the onset of detonation. Testing was conducted with six ramps mounted centerline on both the top and bottom of the mounting plate. Numerous testing was required in order to capture the detonation event located behind the obstacles. Comparing the same event using the different cameras validated that the bright light visible was due to the molecular emission (CH) and was not a shock compression event (Figure 35).
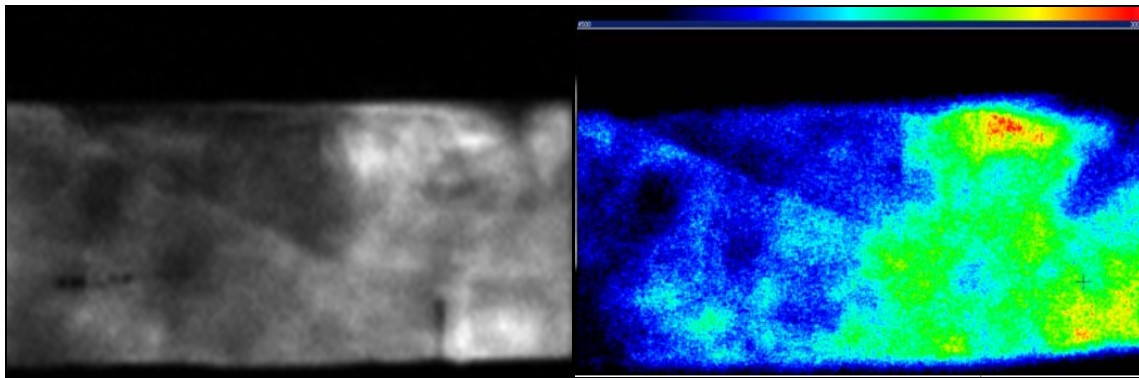
Figure 35.   Capture of Detonation Behind 6th Ramp (Left); Corresponding Image with CH Filter Installed (Right) (φ=1.19)

E.   SUMMARY

The purpose of this testing was not to create detonations using different configurations but to observe the flame front interactions in order to better understand the early development of detonations. Detonations were verified by the resulting shock speeds calculated from the high-speed pressure traces. Different images revealed that bright hotspots were formed along the centerline of the obstacles and approximately 0.5 step heights behind the ramps. Using the appropriate filter, images were taken that indicated that the source of the bright illumination was from a combustion event and not from other sources such as shock heating. To better understand the initiation mechanisms, the detonation images need to be compared to computer simulations of similar conditions.

V.   COMPUTER SIMULATION

Computational Fluid Dynamic (CFD) simulations were used to explore the flow field/chemistry interactions responsible for DDT. The goal of this portion of the research was to better understand the mechanisms required for detonation while using various swept ramp configurations.

Due to the complex chemistry, gas dynamics, and the varying pressure and temperatures occurring during the event, the exact details of the detonation are not entirely understood. This complexity has had the effect of hindering the development of accurate computer models and simulations that would assist in this investigation. The CFD simulations presented in this paper are to mainly illustrate the effect the of the flow field around the obstacles with and without combustion present.

The ramp configurations selected for examination required massive amounts of processor time and memory. A single 3D model typically had more than 9 million elements; due to the large number of input variables and the desired output parameters, the computing power of a single machine was insufficient. Due to this a high-performance computing cluster consisting of 32 individual quad-core machines running the ANSYS software package CFX was used to decrease the solution time. The required time for solution varied greatly depending on the type of solution, steady state or transient type, and whether chemistry was being simulated in the model.

A.   MODELING SOFTWARE

Two different software packages were used in the computer simulation process. SolidWorks 2008 was utilized and is developed by Dassault Systèmes SolidWorks Corporation. The second software package employed was ANSYS CFX and was designed by ANSYS, Inc. Both of these software packages run on a Windows operating system; additionally, CFX ran on the cluster that was a Linux operating system.

1.   SolidWorks

SolidWorks 2008 was used to draw 3D combustor models used in the computer simulation. SolidWorks is a 3D mechanical CAD software package that is a parasolid based modeler and incorporates a parametric based approach used to create models.

The combustor and swept ramp obstacles were drawn to accurately simulate the actual conditions of the experimental test assembly. Various combustor lengths were used depending on the ramp configuration in order to produce valuable simulations on a practical time scale. Based on successful experimental results, two different ramp configurations were selected for further analysis using computer simulation.

The challenge in modeling the combustor was visualizing the volume available for the reactants to occupy. In order to create this type of geometric model a drawing of the internal volume of the combustor was drawn (Figure 36) as well as the desired swept ramp obstacle configuration (Figure 37).
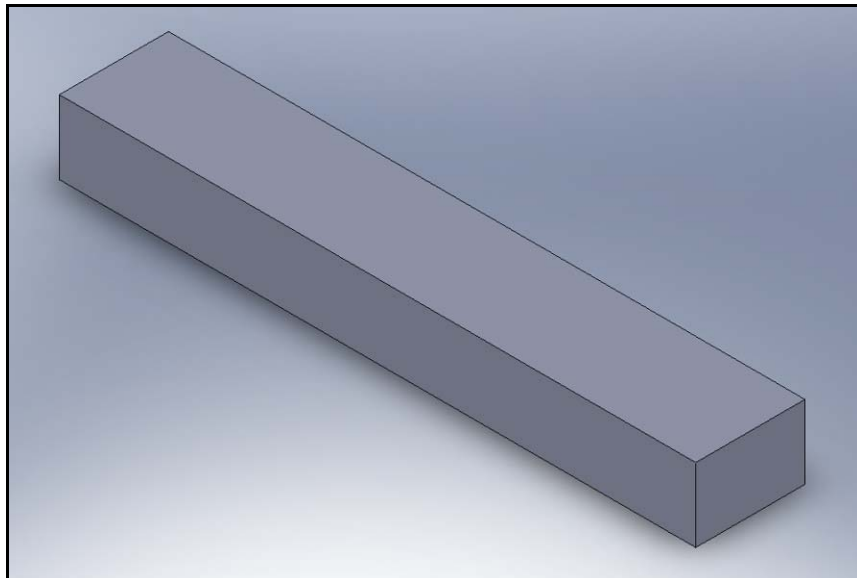
Figure 36.   SolidWorks Drawing of the Internal Volume of the Combustor.
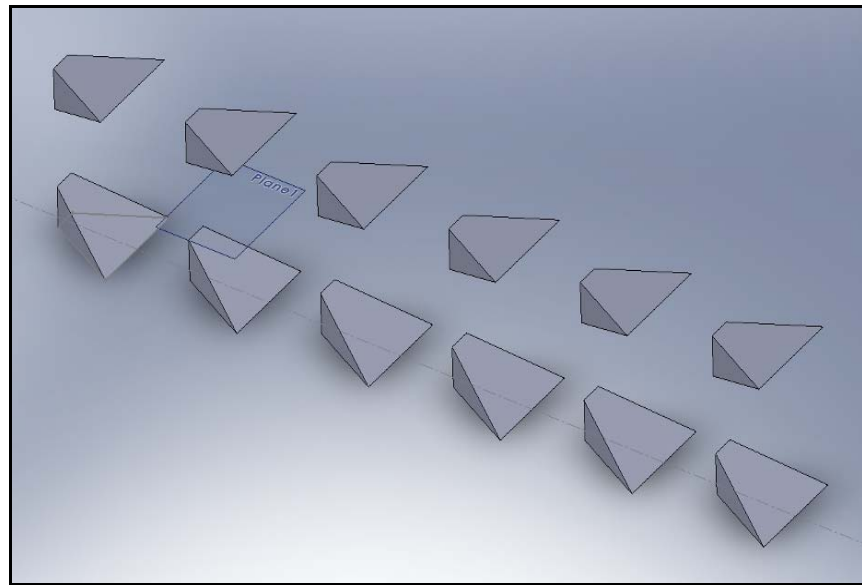
Figure 37.   SolidWorks Drawing of 6 Swept Ramp Stages Located Centerline and on the Top and Bottom of the Combustor.

With these two part drawings, a geometric volume comparison was conducted in SolidWorks which resulted in the total ramp volume removed from the internal volume of the combustor (Figure 38).
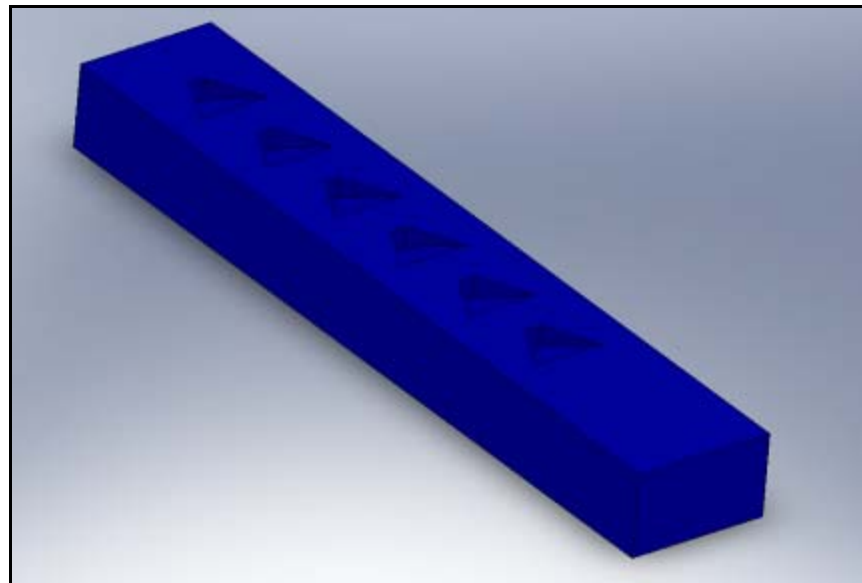
Figure 38.   Volume Comparison Completed from SolidWorks Used in Simulation.

2. ANSYS CFX

ANSYS CFX is a high performance, general purpose Computational Fluid Dynamics (CFD) program that is used to solve various fluid flow problems. ANSYS CFX uses a solver that can be highly parallelized and incorporates a flexible user environment that employs intuitive GUIs.

After the combustor volume was completed in SolidWorks, it was exported into ANSYS CFX. Once imported into CFX-Pre, a volume mesh was generated based on user inputs which control the quality and size of the resulting mesh (Figure 39).
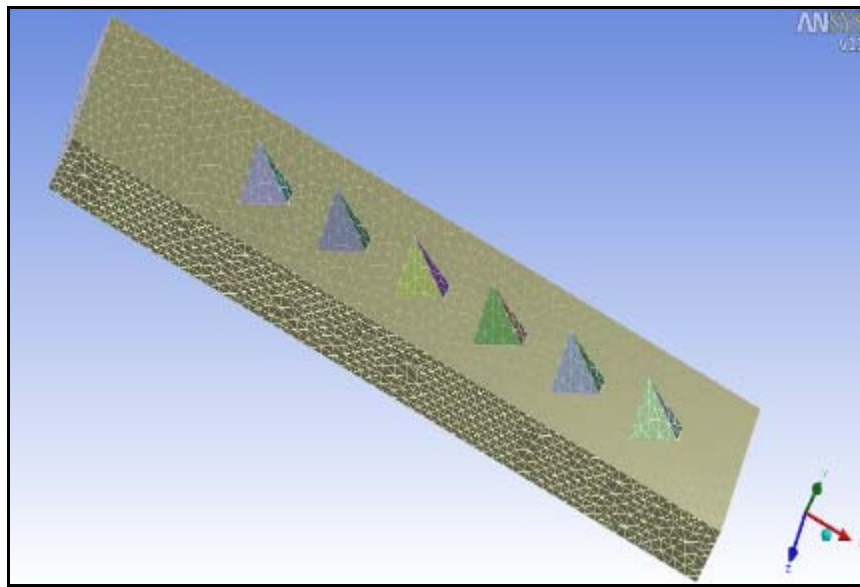
Figure 39.   Example of Volume Mesh Generated in CFX-Pre.

Once an adequate volume mesh was created, CFX-Pre was then used to define the boundary and initial conditions of the flows to be evaluated. All the simulations defined the forward end as the inlet and the aft end as an outlet; all other surfaces were treated as a wall. With this defined simulation, CFX computed a solution of the entire test volume at a time interval defined by the user. CFX-Post was used to view the results in sequence and to conduct post-processing and analysis on the results. Analysis was conducted by creating various planes through the combustor and defining parameters of interest to be

evaluated. These parameters included but were not limited to velocity, pressure, temperature, and turbulence kinetic energy. Figure 40 shows an example of an XY plane cut through the Z-axis of a solution.
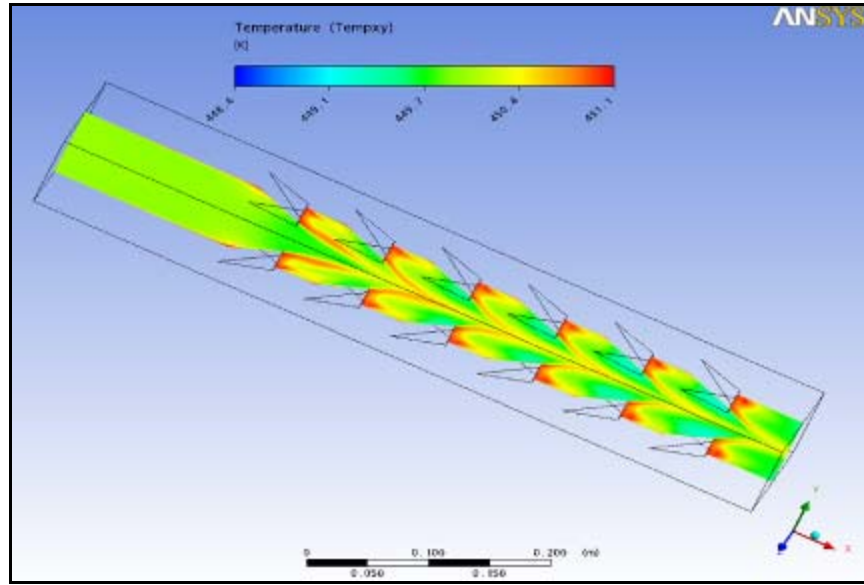
Figure 40.   Example of a Post-Process Temperature Analysis of an XY Plane Slicing Through the Origin.

B.   SIMULATION RESULTS

1.   Swept Ramp Configurations

CFX simulations of several ramp configurations were conducted to obtain steady-state results. The configurations selected were ones that detonations were observed during experimental testing. The configurations considered included five or six swept ramp rows constructed into two different arrangements. The first arrangement consisted of either five or six rows of two (Figure 41) while the second layout was either five or six rows of a single ramp located centerline with an opposing ramp located on the opposite face (Figure 42). The obstacles used had a maximum height of 19.43 mm and a sweep angle of approximately 63 degrees. The exact dimensions of the obstacles used are found in Appendix A. The typical initial conditions in the test volume and at the outlet were set for approximately sea level conditions to include a static pressure of 1 atm and temperature of 450 K. Air modeled as an ideal gas was simulated to flow into the inlet

51

with an initial mass flow rate of 0.3125 kg/s. The wall was simulated as an adiabatic surface with no slip conditions established for flow. A summary of the CFX steady-state simulations and the parameters used for the initial and boundary conditions are included in Table 2 and Table 3.
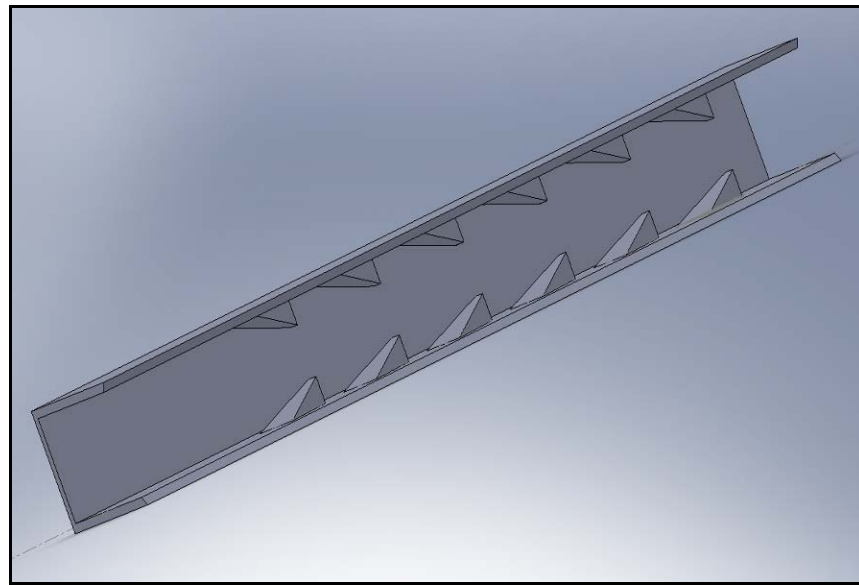
Figure 41. Cutaway of Simulation Configuration of 6 Rows of Ramps Centerline/Opposing.
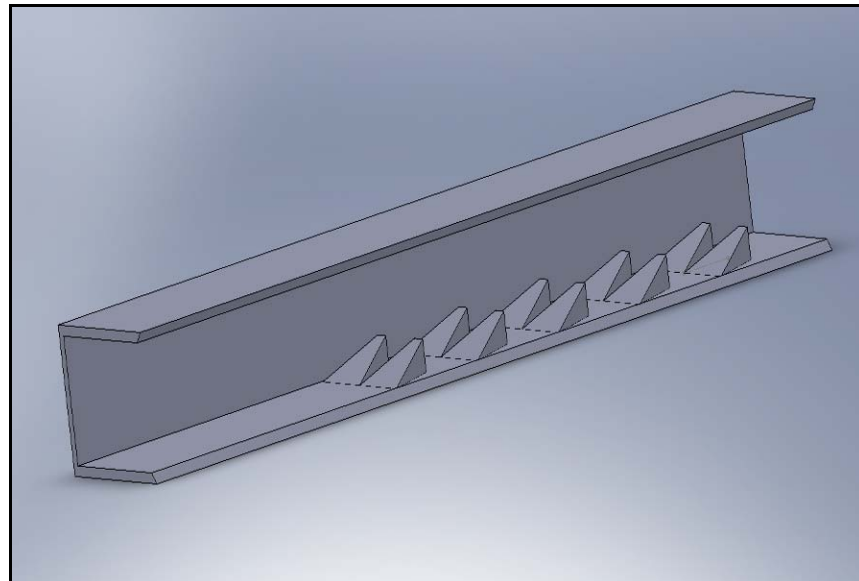
Figure 42. Cutaway of Simulation Configuration of 6 Rows of 2 Ramps.

Table 2.   Steady-State CFX Configurations with Resulting Volume Mesh Information.

Configuration	Ramps per Row	No of Rows	No of Nodes	No of Elements
5 Rows of 2	2	5	2475988	8756895
6 Rows of 2	2	6	2454757	8709301
5 Rows Centerline/Opposing	1	5	2605670	8961295
6 Rows Centerline/Opposing	1	6	2621557	8974794

Table 3.   Steady-State CFX Initial and Boundary Conditions.

Location	Type	Conditions	
Inlet	Inlet	Flow Direction:	Normal to Boundary Condition
		Flow Regime:	Subsonic
		Heat Transfer:	Static Temperature
		Static Temperature:	450[K]
		Mass Flow Rate:	0.3125 [kg/ s]
		Mass And Momentum:	Mass Flow Rate
		Eddy Length Scale:	0.02 [m]
		Fractional Intensity:	0.01
		Turbulence:	Intensity and Length Scale
Outlet	Outlet	Flow Regime:	Subsonic
		Mass And Momentum:	Average Static Pressure
		Pressure Profile Blend:	0.05
		Relative Pressure:	0 [Pa]
		Pressure Averaging:	Average Over Whole Outlet
Wall	Wall	Heat Transfer:	Adiabatic
		Mass And Momentum:	No Slip Wall
		Wall Roughness:	Smooth Wall

2.   Steady-State Results

ANSYS CFX was used to determine the steady-state results for the configurations listed in Table 2. Post-processing on CFX allowed multiple planes to be inserted at various locations of the combustor displaying a wide variety of parameters. Turbulence Kinetic Energy (TKE) as well as shear strain rate were used for insight in understanding the causes of detonations since areas of high TKE and shear strain rate were correlated to very reactive locations observed during experimental testing. TKE is the average kinetic

energy of the fluctuating velocity components in turbulent flow. The shear strain rate of a fluid is defined as the rate of decrease of the angle formed by two perpendicular lines in the fluid. Areas of high shear strain rate act as a viscous boundary and thus have the ability to direct/divert flow. Figures 43-47 were created from the steady state simulation with 6 stations of inline and opposing ramps (Figure 41).
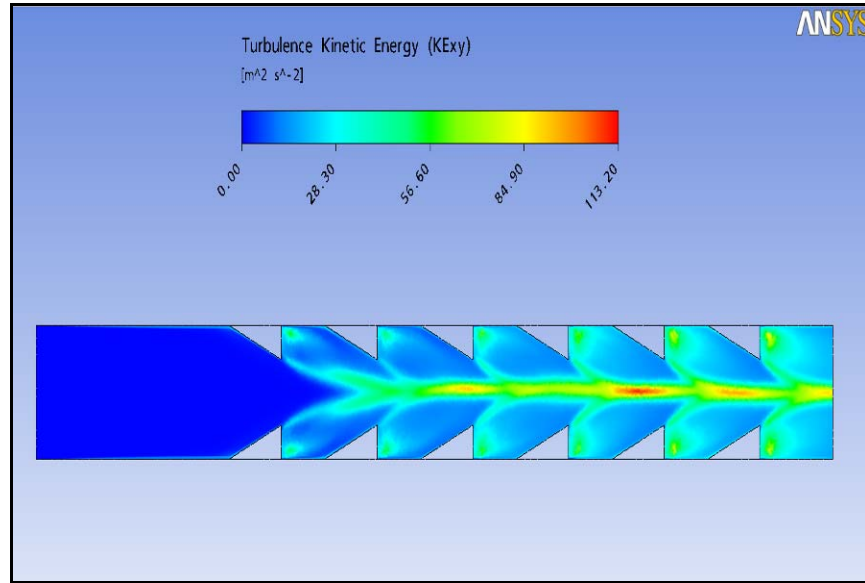
Figure 43.   Centerline Turbulence Kinetic Energy of 6 Ramp Rows Inline/Opposing.
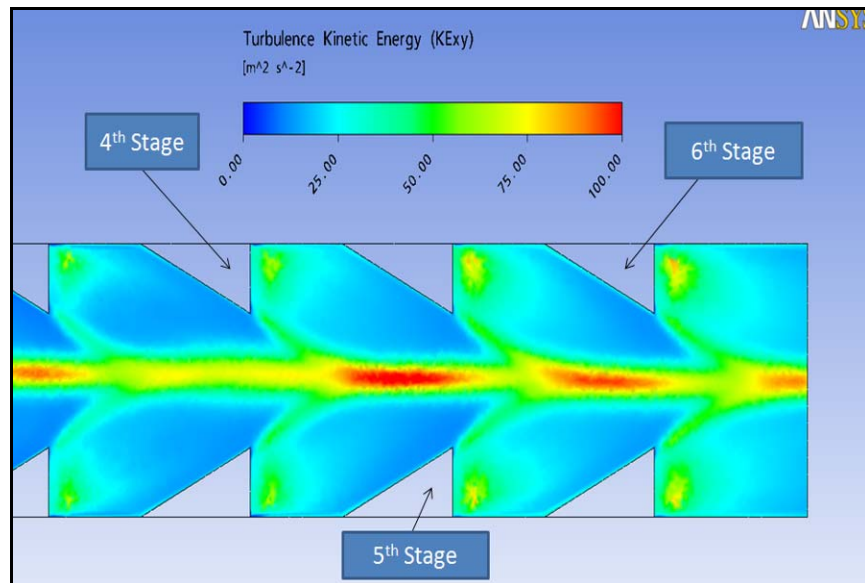
Figure 44.   Centerline Turbulence Kinetic Energy in the 4th-6th Stages.
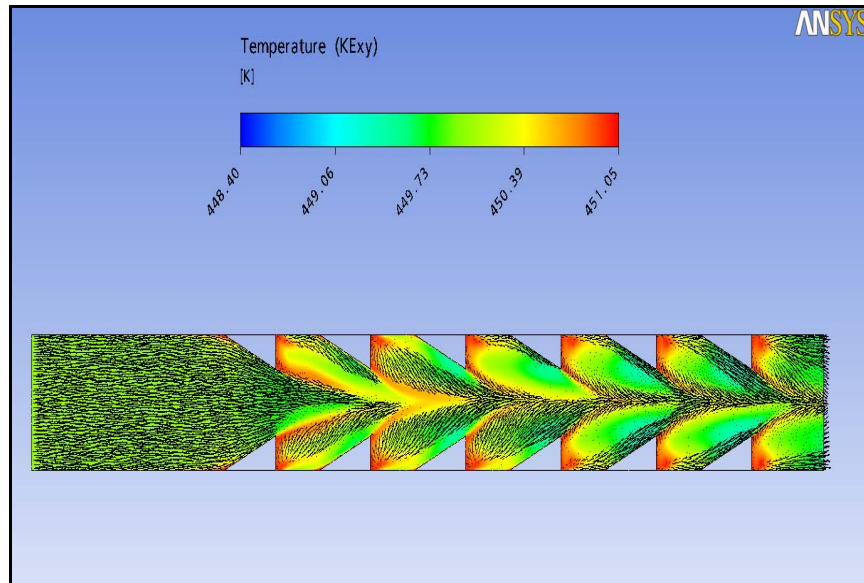
Figure 45.   Centerline Temperature Plot with Velocity Vectors of 6 Ramp Rows
Inline/Opposing.

Figure 43 and 44 are centerline plots of the TKE in the combustor. Theses plots reveal an increase of TKE directly behind the swept ramps which grows in intensity down the combustor. Figure 45 is a centerline plot of temperature, which shows an increase in temperature behind each ramp, also growing in intensity down the combustor.
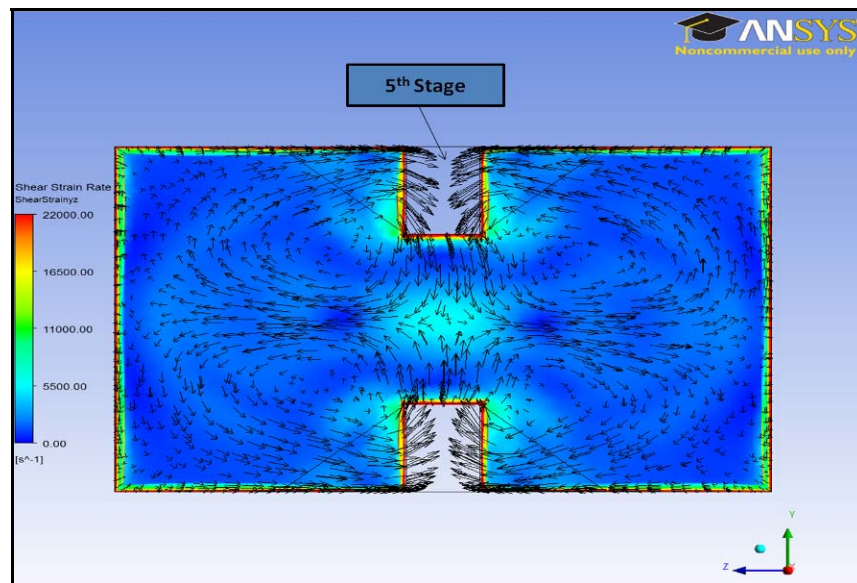
Figure 46.   Shear Strain Energy with Velocity Vectors (Located at Base of 5th Ramp).
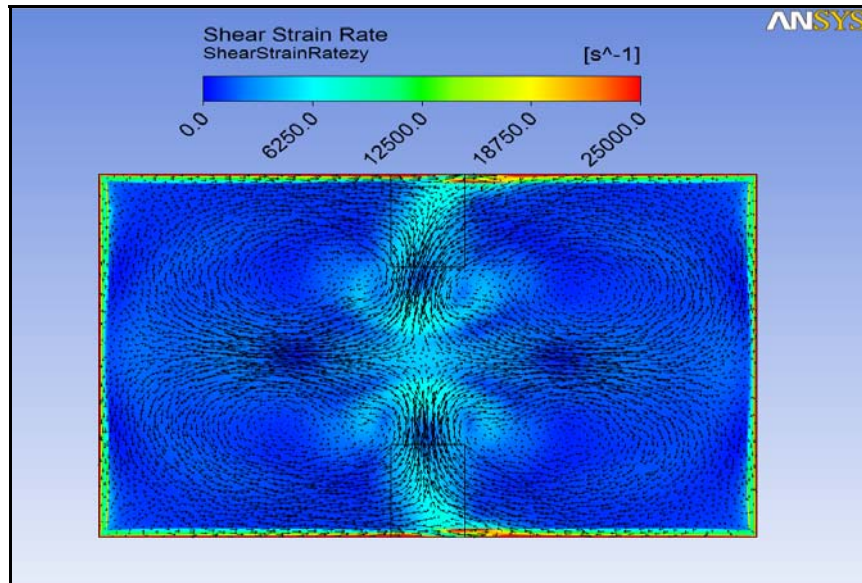
Figure 47.   Shear Strain Energy with Velocity Vectors (Located 2.54 cm Downstream of 5th Ramp).

Figure 46 and 47 are plots of shear strain rate at different locations in the combustor. Both figures reveal a high shear strain rates directly behind the ramps, caused by the symmetrical vortexes that are created by the flow field rolling off each edge of the swept ramp.

Figures 48 through 50 are plots of the steady state simulation of 6 rows of 2 ramps side by side (Figure 42). Figure 48 shows the centerline TKE down the length of the combustor; this plot reveals an increase in TKE behind each ramp station, which also increases in intensity down the combustor.
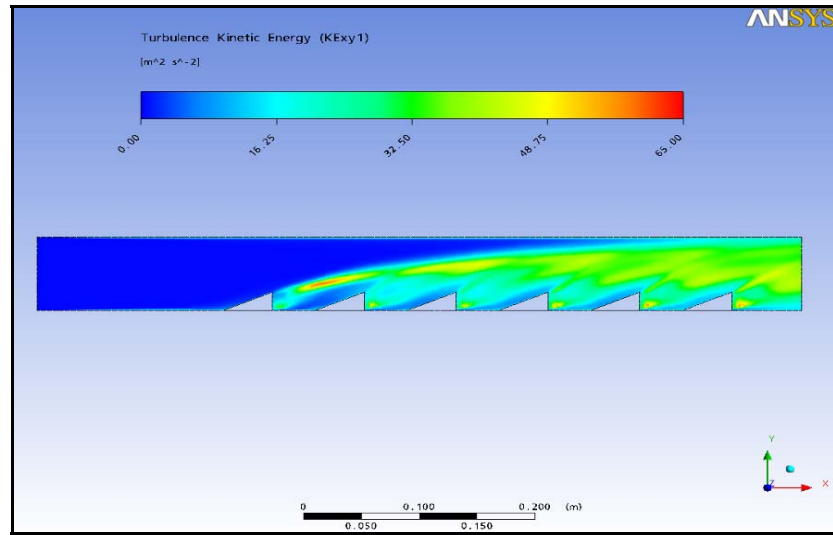
Figure 48.   Centerline Turbulence Kinetic Energy of 6 Rows of 2 Ramps.

Figures 49 and 50 plot the TKE at various locations; both reveal areas of high TKE behind the ramps and each slanted toward the outboard of the combustors. These plots show the resulting flow fields due to the steady state flow interactions between the two ramps and the center channel. The resulting flow fields due to the ramps were symmetrical along each station. All of the steady state simulations indicated areas of high TKE and temperature behind each obstacle, increasing in intensity down the combustor.
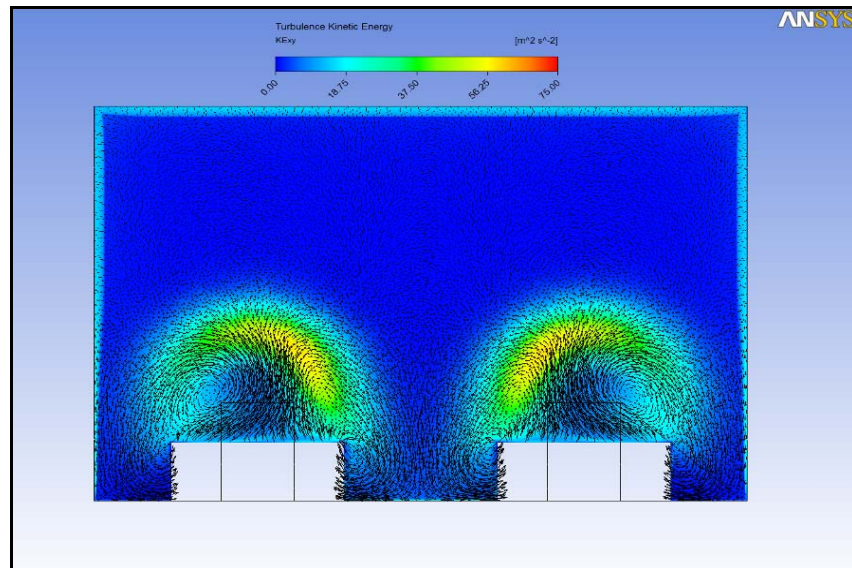
Figure 49.   Turbulence Kinetic Energy with Velocity Vectors @ Halfway Up 2nd Set of Ramps.
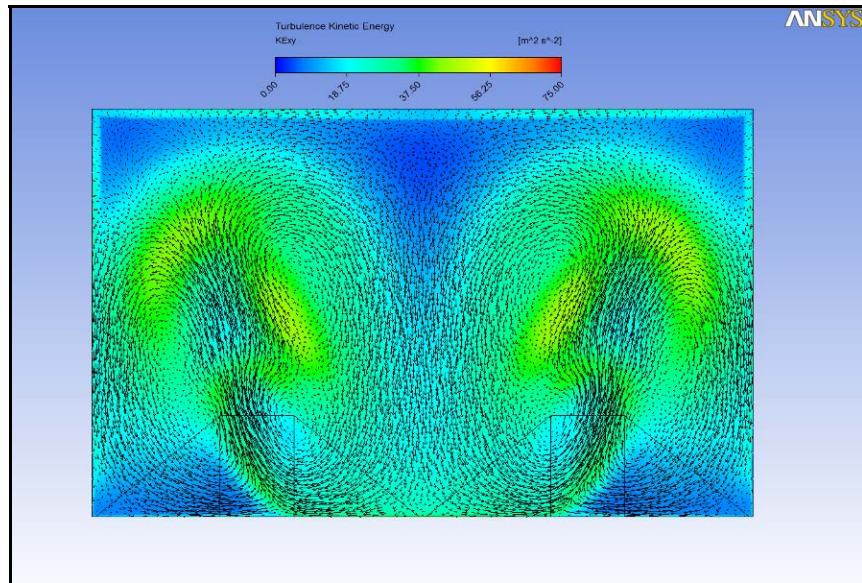
Figure 50.   Turbulence Kinetic Energy with Velocity Vectors Midway between 5th and 6th Ramps.

3.   Transient Results with Chemistry Simulated

CFX simulations of several ramp configurations were conducted to obtain transient chemistry results. The transient simulation was initialized with the Ethylene/Air mixture model including all the products of combustion. Nitrogen gas was suppressed, which restricted the combustion to a modified ethylene/oxygen mixture. Combustion was modeled using finite rate chemistry including the eddy dissipation model and turbulence was computed with the standard k-epsilon model. The reference pressure and temperature were set to standard conditions. The reduced ethylene/air chemistry model used was based on that used by Foreman Williams of the University of California San Diego (UCSD) [11]. Initial inlet boundary total pressure was 2.7 atmospheres and 2,800K static temperature with the products of combustion being introduced at 600 m/s. The outlet boundary was set to subsonic conditions at 3.0 atmospheres and the composition was a mixture of ethylene and oxygen. Initially the combustor was filled with an ethylene/ oxygen mixture, once the simulation was started only the designated products were injected into the inlet. By injecting only the products, an ideal combustion event was created with only the designated products remaining in the wake of the combustion wave. An Arrhenius reaction rate with adequate activation energy was assigned to ensure a

proper rate of reaction took place. The transient simulation used an adaptive time step using RMS Courant number. To ensure adequate convergence, a value of four for the Courant number was chosen for these simulations. A maximum of 75 iterations per time step was selected to allow the simulation to converge.

Based on the complexity of the simulation, the entire obstacle model could not be simulated. Since the entire obstacle configuration could not be analyzed, detonations were not generated in the simulation, but the fuel/air mixture flow fields could be examined at locations where the experimental results revealed strong reaction sites. In order to get a representation of the mechanisms required for initiating detonation and to simplify the simulation, two configurations were analyzed. A summary of the CFX transient simulations and the parameters used for the initial and boundary conditions are included in Table 4 and Appendix B. The first transient simulation consisted of one station of 2 ramps mounted side by side mounted on the bottom of the test area (Figure 51).
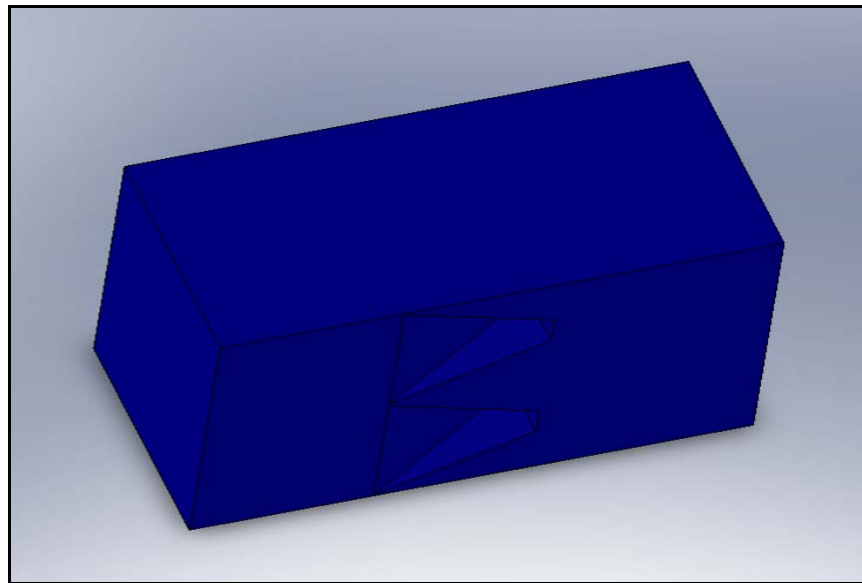
Figure 51.   Transient Chemistry Simulation Model with 1 Station of Side by Side Ramps.

Table 4.   Transient Chemistry CFX Configurations with Resulting Volume Mesh Information.

Configuration	Ramps per Row	No of Rows	No of Nodes	No of Elements
Single Station; 1 Row of 2	2	1	2475988	8756895
Two Station; 2 Ramps Inline/Opposing	1	2	2454757	8709301

Figure 52 represents the position of the flame front at various times as it passed over the middle of the ramp. The first time step behind the ramp revealed the absence of fuel since the flame front had been accelerated behind the ramps. Figure 53 are plots of the shear strain rate downstream of the ramp station and indicate the flow path. Figure 53 revealed that a strong vortex was created due to the flow field rolling off the outboard edge of the ramps. A strong vortex was also created down the centerline of the combustor ramp located between the ramps; the interaction between these vortexes occurred directly behind the ramps as indicated by an area of high TKE which corresponded to observed regions of very rapid reactions (explosions). Figure 54 is a 3D representation of the vortexes created from the combustion event and from the interactions with the side by side ramp obstacles.
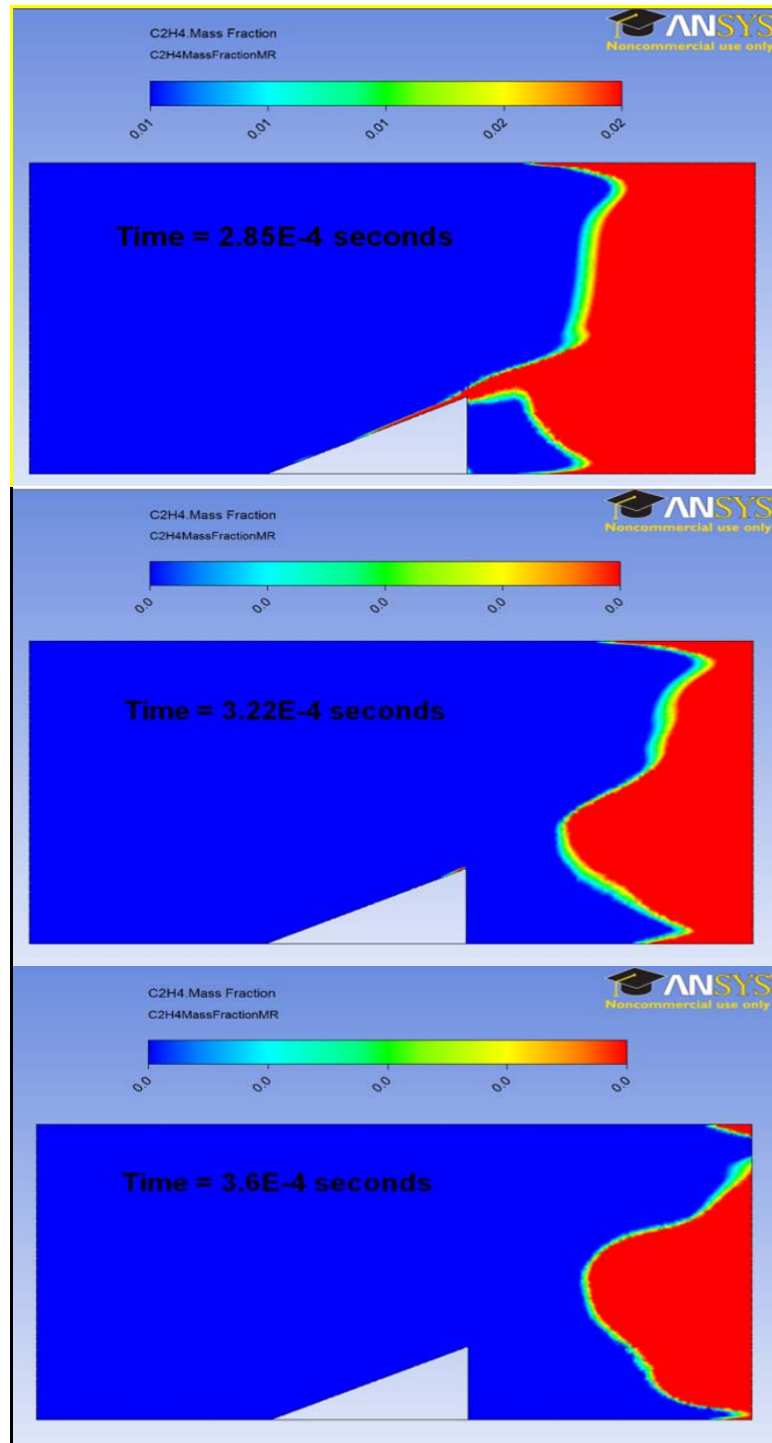
Figure 52.   Ethylene Mass Fraction Along the Centerline of a Ramp at Various Times.
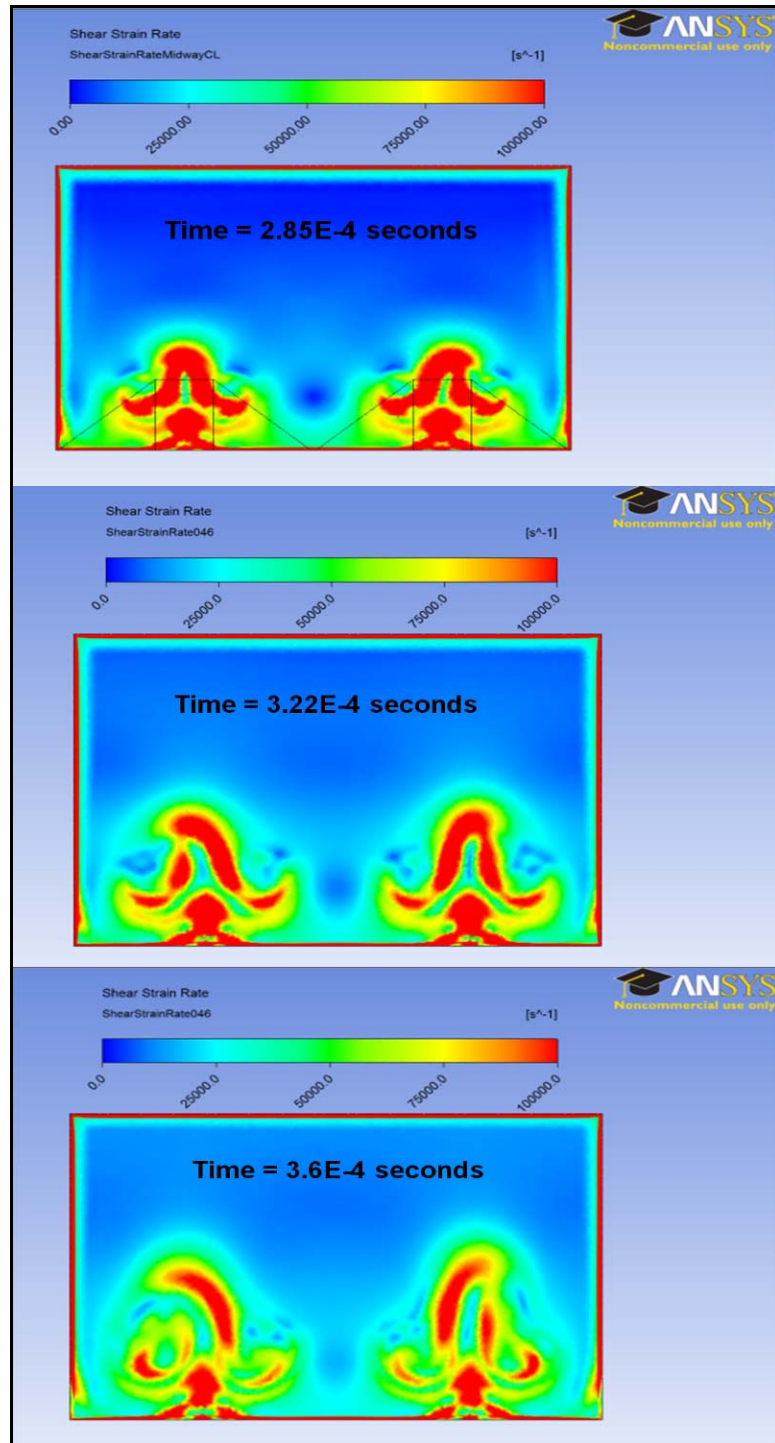
Figure 53.   Shear Strain Rate 1.4 cm Downstream the Ramp Station at Various Times.
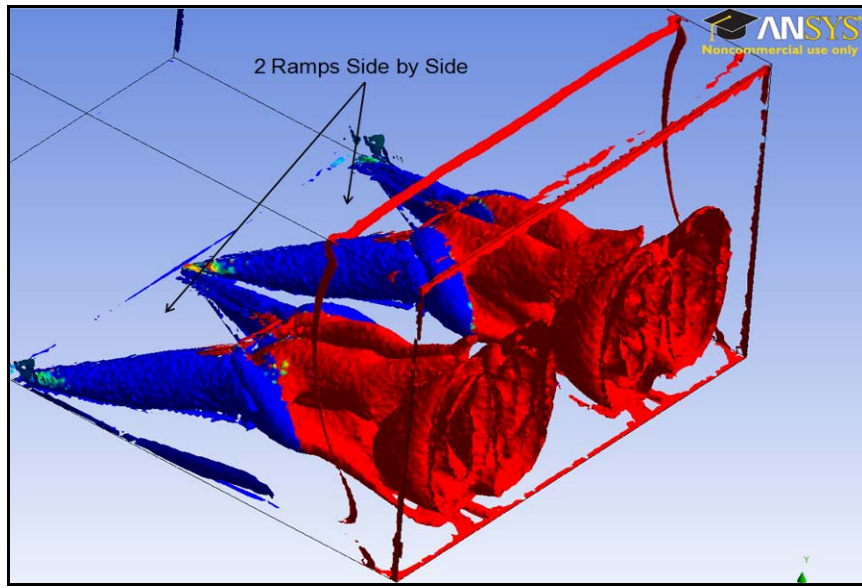
Figure 54.   Ethylene Mass Fraction Vortexes at Time 3.22E-4 sec.

After the results from this model were examined, a second arrangement was created in order to show the interactions between multiple stations of ramps. This second configuration consisted of 2 stages of inline ramps mounted along the centerline on the top and bottom of the test area (Figure 55). For this second configuration, the number of elements in this model had to be reduced in order for the high-performance computing cluster to produce results.
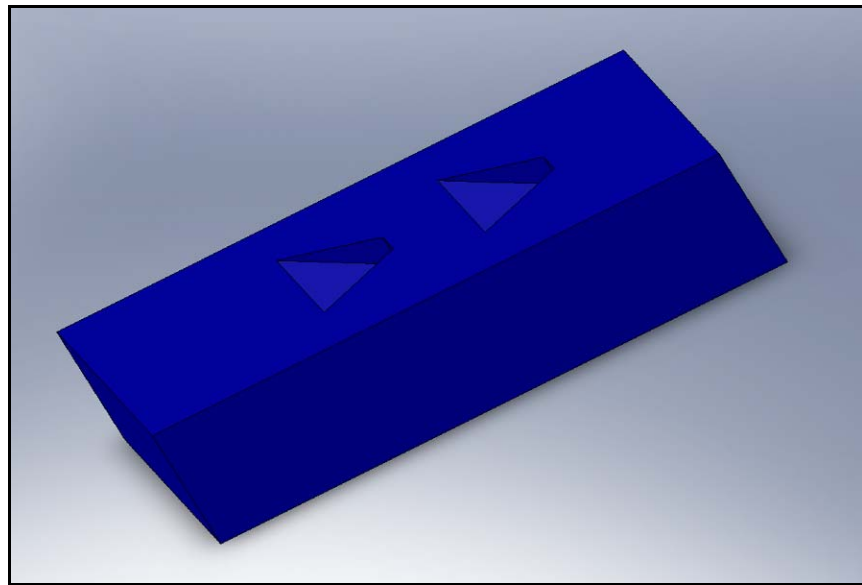
Figure 55.   Transient Chemistry Simulation Model with 2 Stations of Inline/Opposing Ramps.

Figures 56 and 57 revealed a snapshot in time of the differing axial positions of the flame front. Figure 57 indicated that the flame front along the wall was traveling at a higher velocity that the flame front along the centerline. The flame front was accelerated behind the swept ramps due to the flow fields rolling off the edges of the swept ramps represented by the presence of combustion products present behind the ramps (Figure 56). This difference in velocities explained the appearance in the images that the flame front had already passed the detonation site. A comparison was conducted between the simulation results and the images recorded from actual testing (Figure 58). This comparison revealed that flame front along the wall and the flame front behind the ramps were moving close to the same velocity, thus creating a 2D image that the flame front had passed the detonation site and then collapsed back toward it.
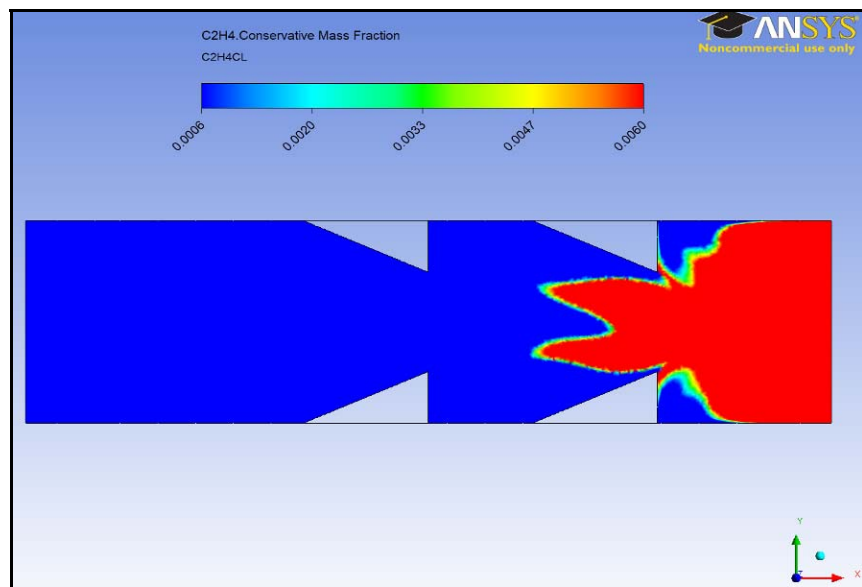
Figure 56.   Ethylene Mass Fraction along Centerline at Time 6.31E-4 sec.
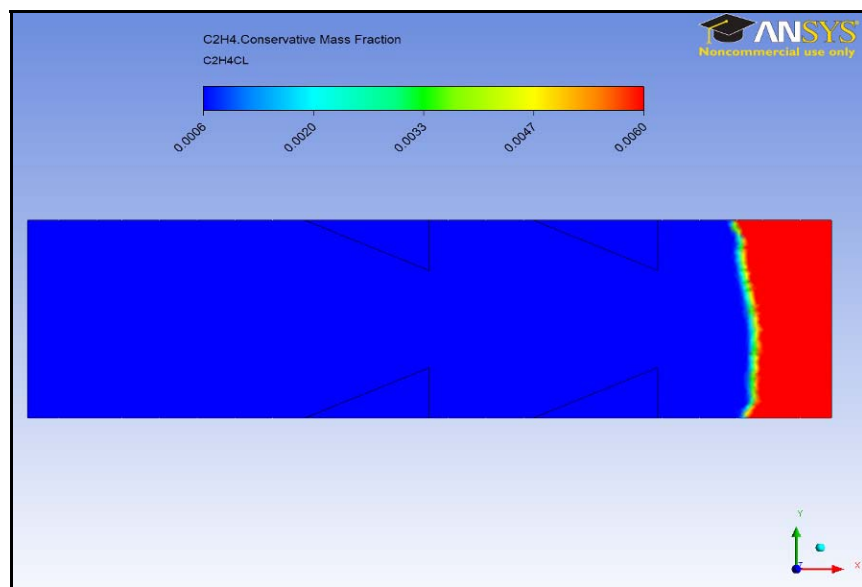
Figure 57.   Ethylene Mass Fraction along the Wall at Time 6.31E-4 sec.
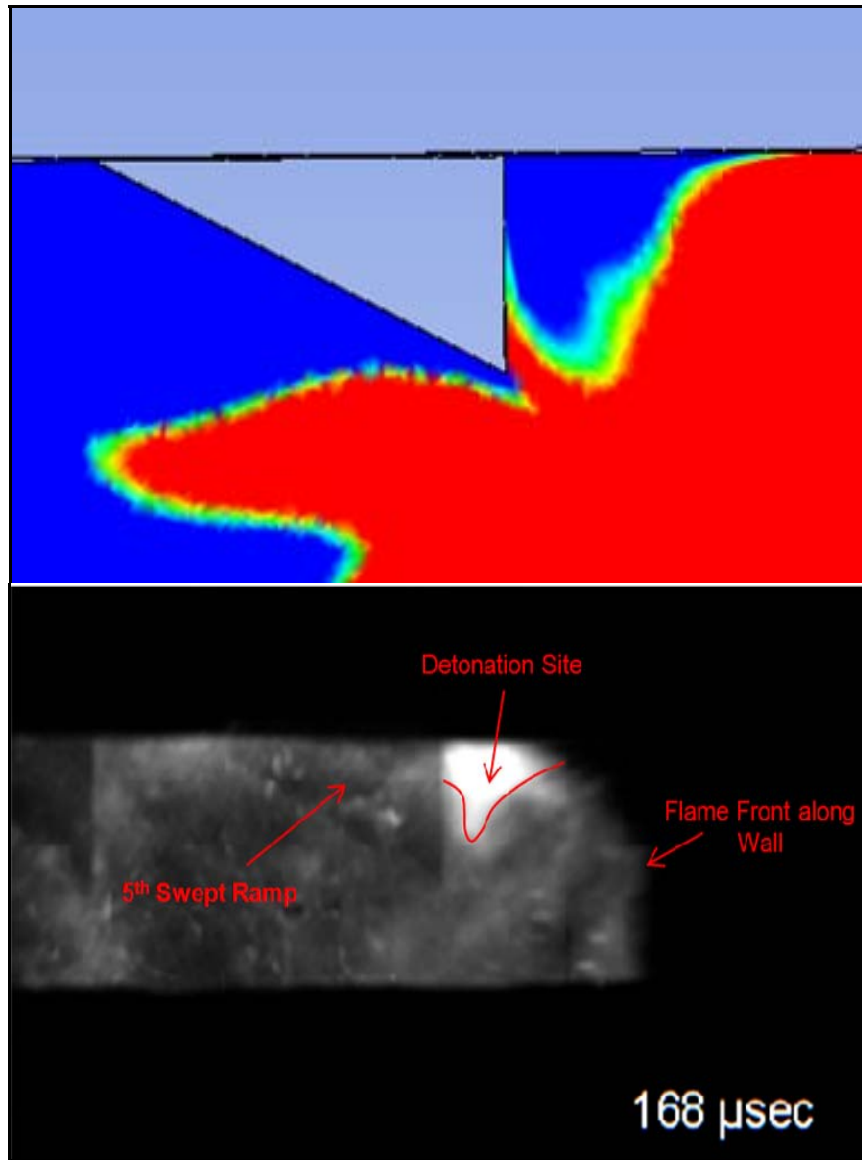
Figure 58.　　　Comparison of Shape of Detonation Site with Actual Image versus Ethylene Mass Fraction along the Centerline.

Figures 59 through 62 indicated that the rolling vortexes off each swept ramp was not symmetrical, but actually a dominant vortex off one side of each of the ramps caused a global rotation of the entire flow fields. The interactions between the flow field off the ramp edge and from the upstream ramps created areas of high TKE directly behind the ramps and correlated to observed detonation initiation locations in actual testing.
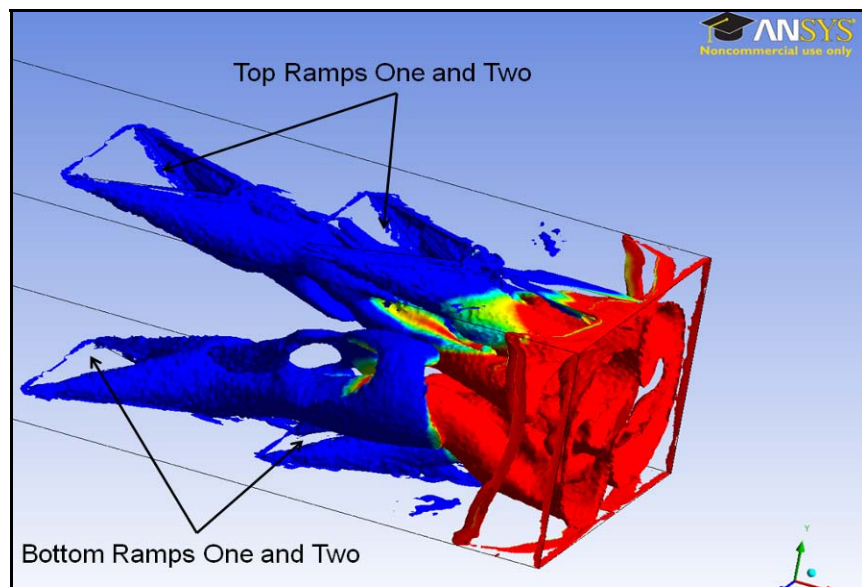
Figure 59.	Ethylene Mass Fraction Vortexes at Time 6.31E-4 sec.
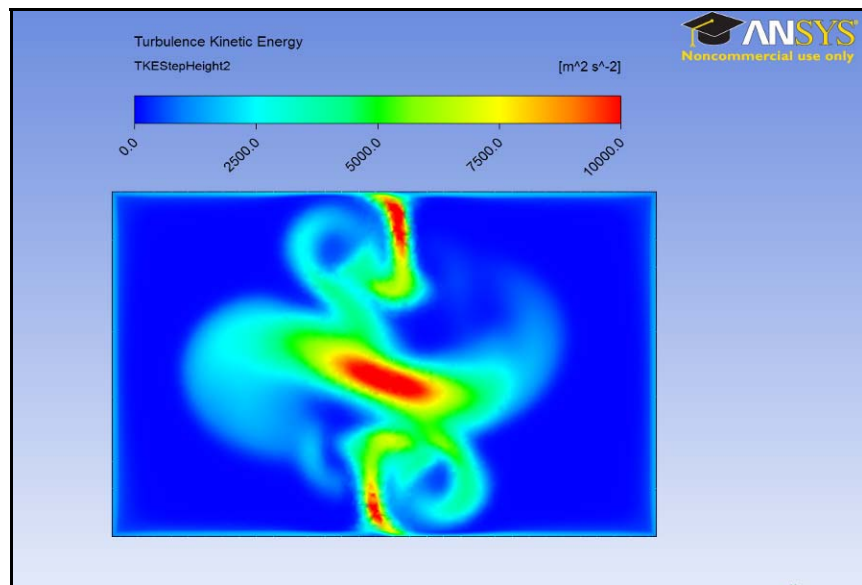
Figure 60.	Turbulence Kinetic Energy 0.4 cm behind 2nd stage at Time 6.31E-4 sec.
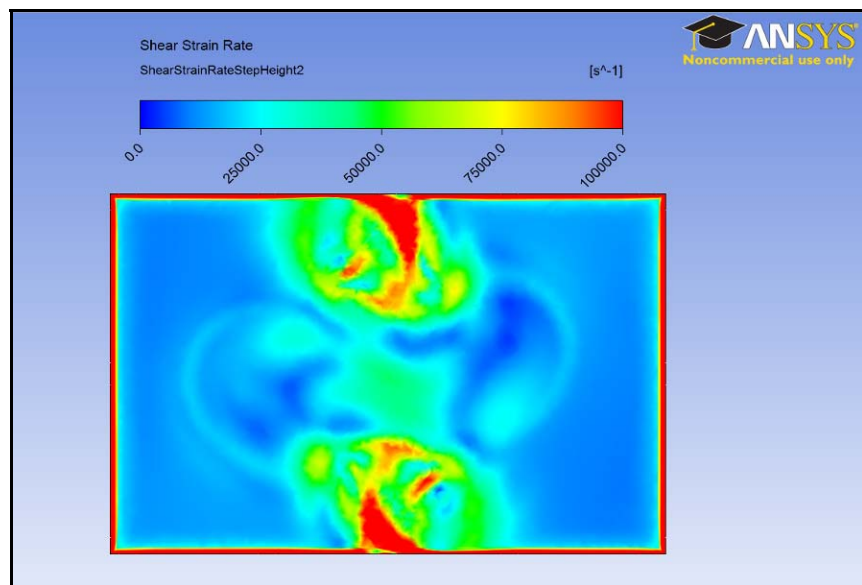
Figure 61.   Shear Strain rate 0.4 cm behind 2nd stage at Time 6.31E-4 sec.
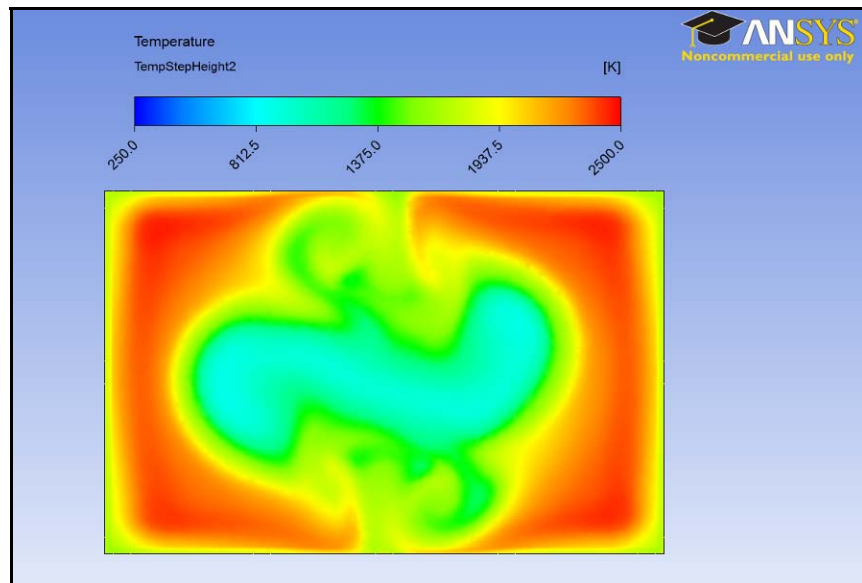
Figure 62.   Temperature 0.4 cm behind 2nd stage at Time 6.31E-4 sec.

VI. CONCLUSIONS AND FUTURE WORK

A. CONCLUSIONS

This thesis explored the fluidic/combustion mechanisms for swept ramp obstacles that are responsible for initiating a detonation event through experimental testing and computer simulation. The experimental testing revealed where the detonations occurred relative to the installed obstacles. The images revealed that the initiation sites for detonation occurred directly behind the ramps and within approximately one half of its step height. The orthogonal integrated view of the detonation event indicated that the flame front had passed the detonation site prior to the detonation event. This observation indicated the possibility of the flame front actually collapsing back into the detonation site and then the creation of the detonation.

Computer simulations were created in an attempt to provide additional qualitative information about the observations from testing but more importantly create a simulation where multiple parameters could be analyzed at various locations in the flow fields that were not achievable through experimental testing. The initial simulations were without combustion and used the entire obstacle configuration. These simulations revealed the flow fields that were created from the interactions with the various obstacle configurations. The final type of simulations analyzed included the introduction of reduced chemistry for the ethylene/oxygen mixture. The simulations including chemistry indicated that the combustion process altered the flow fields at locations behind the swept ramps that were represented by areas of high TKE. After further analysis, the simulation revealed that the flame front did not collapse back toward the location of detonation. The results showed that the rolling flow field off of the swept ramps interacted with the global flow fields created sites that are favorable for detonation.

B. FUTURE WORK

The experimental results of this thesis show that areas of high TKE are precursors for detonation. Further refinement of the chemistry model and adjusting the maximum time steps will produce more precise results. A better method of developing an adequate

volume mesh is needed in order to facilitate simulating the entire obstacle and also allow a more detailed investigation of the combustion events occurring after the ramps. Currently the mesh needed to produce results with adequate quality is greater than the capacity of the high-performance computing cluster. Future simulations could be conducted on different software thus allowing a more exact solution.

APPENDIX A: OBSTACLE DRAWINGS

The drawing contained in this Appendix details the design of the swept ramp obstacle utilized in this research.
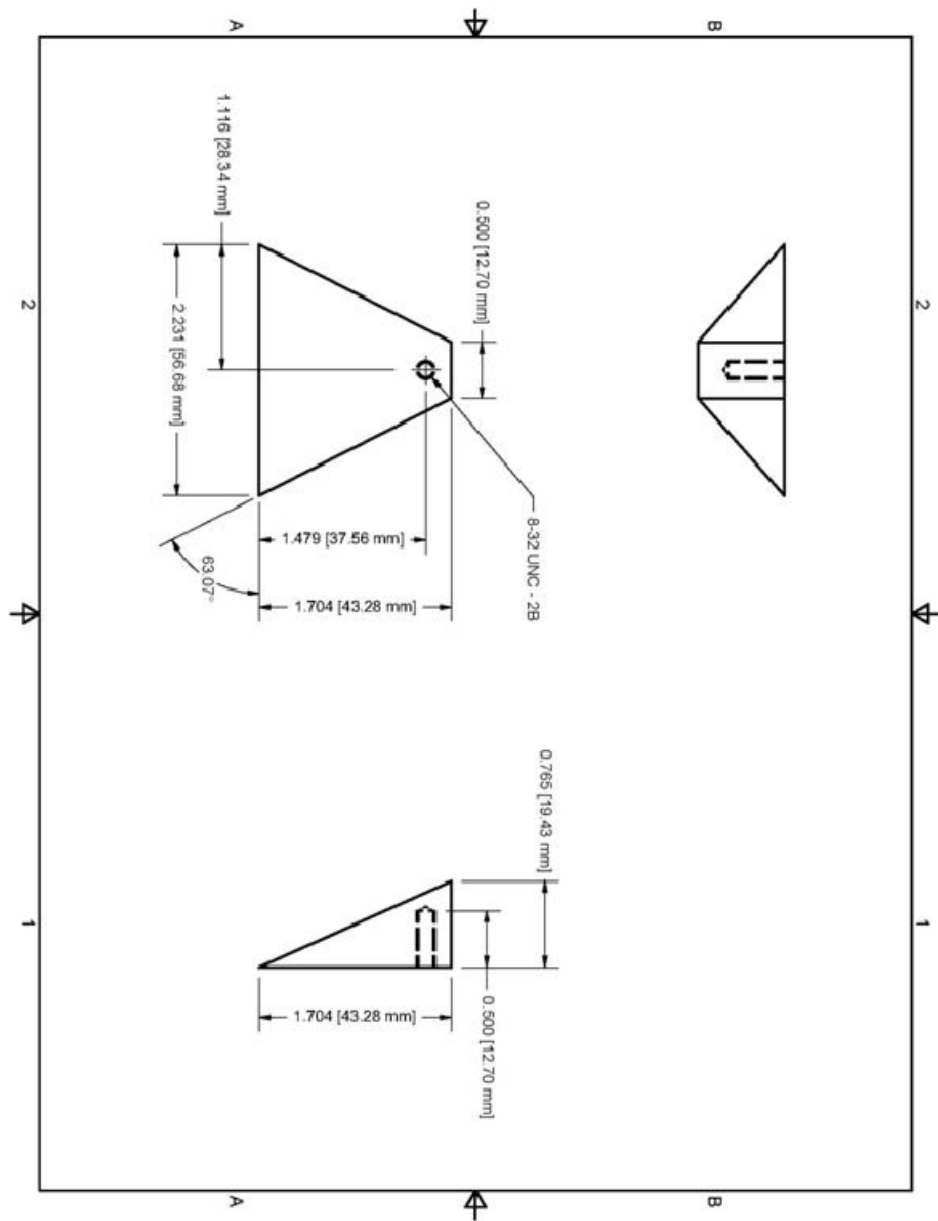
1. Design Details for the Swept Ramp Obstacles [3].

THIS PAGE INTENTIONALLY LEFT BLANK

APPENDIX B: TRANSIENT SIMULATION INITIAL
CONDITIONS

Table 1. Domain Physics

Domain - Default Domain	
Type	Fluid
Location	B34
Materials	
Ethylene Air Mixture	
Fluid Definition	Material Library
Morphology	Continuous Fluid
Settings	
Buoyancy Model	Non Buoyant
Domain Motion	Stationary
Reference Pressure	1.0000e+00 [atm]
Combustion Model	Finite Rate Chemistry and Eddy Dissipation
Eddy Dissipation Model Coefficient B	5.0000e-01
Component	C2H4
Option	Automatic
Component	CO
Option	Automatic
Component	CO2
Option	Automatic
Component	H
Option	Automatic
Component	H2O
Option	Automatic
Component	N2
Option	Constraint
Component	O2
Option	Automatic
Component	OH

Option	Automatic
Heat Transfer Model	Total Energy
Thermal Radiation Model	P 1
Spectral Model	Gray
Turbulence Model	k epsilon
Turbulent Wall Functions	Scalable

Table 2. Boundary Physics

Domain	Boundaries	
Default Domain	**Boundary - Inlet**	
	Type	INLET
	Location	Inlet
	Settings	
	Component	C2H4
	Mass Fraction	0.0000e+00
	Option	Mass Fraction
	Component	CO
	Mass Fraction	4.0873e-02
	Option	Mass Fraction
	Component	CO2
	Mass Fraction	1.3498e-01
	Option	Mass Fraction
	Component	H
	Mass Fraction	0.0000e+00
	Option	Mass Fraction
	Component	H2O
	Mass Fraction	7.1727e-02
	Option	Mass Fraction
	Component	O2
	Mass Fraction	1.6936e-02
	Option	Mass Fraction
	Component	OH
	Mass Fraction	7.7709e-03
	Option	Mass Fraction

Flow Regime	Mixed	
Blend Mach Number Type	Normal Speed	
Heat Transfer	Static Temperature	
Static Temperature	2.8000e+03 [K]	
Mass And Momentum	Cartesian Velocity Components and Total Pressure	
Relative Total Pressure	2.7000e+00 [atm]	
U	6.0000e+02 [m s^-1]	
V	0.0000e+00 [m s^-1]	
W	0.0000e+00 [m s^-1]	
Thermal Radiation	Local Temperature	
Turbulence	Low Intensity and Eddy Viscosity Ratio	
Boundary - Outlet		
Type	OPENING	
Location	Outlet	
Settings		
Component	C2H4	
Mass Fraction	6.3744e-02	
Option	Mass Fraction	
Component	CO	
Mass Fraction	0.0000e+00	
Option	Mass Fraction	
Component	CO2	
Mass Fraction	0.0000e+00	
Option	Mass Fraction	
Component	H	
Mass Fraction	0.0000e+00	
Option	Mass Fraction	
Component	H2O	
Mass Fraction	0.0000e+00	
Option	Mass Fraction	
Component	O2	

	Mass Fraction	2.1815e-01
	Option	Mass Fraction
	Component	OH
	Mass Fraction	0.0000e+00
	Option	Mass Fraction
	Flow Regime	Subsonic
	Heat Transfer	Opening Temperature
	Opening Temperature	2.9800e+02 [K]
	Mass And Momentum	Entrainment
	Relative Pressure	3.0000e+00 [atm]
	Thermal Radiation	Local Temperature
	Turbulence	Zero Gradient
	Boundary - Wall	
	Type	WALL
	Location	Wall
	Settings	
	Heat Transfer	Adiabatic
	Mass And Momentum	No Slip Wall
	Thermal Radiation	Opaque
	Diffuse Fraction	1.0000e+00
	Emissivity	5.0000e-01
	Wall Roughness	Rough Wall
	Sand Grain Roughness Height	2.0000e+01 [micron]

APPENDIX C: CEQUEL CALCULATIONS AND TABLES

CEQUEL was used to determine the mass flow rates necessary to achieve the various equivalence ratios during testing. Based on the required mass flow rates and the choke size installed in the piping, a pressure was determined that could be entered into the ER3000 for both air and ethylene. Both the air and fuel pressure gages were calibrated prior to testing to ensure that correct mass flow rate would be delivered in order to prevent any misinterpretation of data.

P	1	BAR
T	290	K
a	341.18230002	m/s
A	0.008437	m^2

φ	Mol WT	R	RHO	P/P1	T/T1	RHO/RHO1	Det Mach a	Fuel %	Det Vel (m/s)
0.8	28.73171	289.383	1.19160	16.33845	9.07435	1.78726	5.01005	4.67983	1709.34
0.9	28.72767	289.424	1.19143	17.31529	9.48006	1.80014	5.14446	5.23419	1755.20
1.0	28.72368	289.464	1.19126	18.02134	9.74353	1.80305	5.24457	5.78214	1789.35
1.1	28.71974	289.504	1.19110	18.47211	9.88352	1.80795	5.31618	6.32379	1813.79
1.2	28.71584	289.543	1.19094	18.66639	9.91431	1.80176	5.36280	6.85925	1829.69
1.3	28.71199	289.582	1.19078	18.71292	9.85240	1.79178	5.38762	7.38862	1838.16
1.4	28.70819	289.620	1.19062	18.61556	9.72281	1.78128	5.39526	7.91200	1840.77
1.5	28.70442	289.658	1.19046	18.45947	9.55274	1.77233	5.39108	8.42951	1839.34
1.6	28.70070	289.696	1.19031	18.27900	9.36234	1.76623	5.37943	8.94123	1835.37
1.7	28.69703	289.733	1.19016	18.06745	9.16315	1.75956	5.36307	9.44726	1829.79
1.8	28.69339	289.770	1.19001	17.86898	8.96099	1.75481	5.34353	9.94770	1823.12
1.9	28.68979	289.806	1.18986	17.66462	8.75866	1.75067	5.32160	10.44264	1815.64
2.1	28.68272	289.877	1.18956	17.25873	8.35815	1.74336	5.27206	11.41637	1798.73

Mach #	0.05		0.1		0.2		0.3		0.4	
Velocity (m/s)	17.0561		34.1182		68.2365		102.3547		136.4729	
M_DOT Total (kg)	0.1715		0.3430		0.6860		1.0290		1.3720	
M_DOT ---->										
φ	AIR	FUEL	AIR	FUEL	AIR	FUEL	AIR	FUEL	AIR	FUEL
0.8	0.16348	0.00803	0.32596	0.01605	0.65391	0.03210	0.98987	0.04876	1.30762	0.06421
0.9	0.16253	0.00898	0.32505	0.01795	0.65011	0.03591	0.97516	0.05386	1.30021	0.07131
1.0	0.16159	0.00992	0.32317	0.01983	0.64635	0.03967	0.96952	0.05950	1.29270	0.07933
1.1	0.16066	0.01085	0.32132	0.02169	0.64263	0.04338	0.96395	0.06507	1.28526	0.08676
1.2	0.15974	0.01176	0.31948	0.02353	0.63896	0.04706	0.95844	0.07058	1.27792	0.09411
1.3	0.15883	0.01267	0.31766	0.02534	0.63533	0.05069	0.95299	0.07603	1.27066	0.10137
1.4	0.15793	0.01357	0.31587	0.02714	0.63174	0.05428	0.94761	0.08142	1.26347	0.10835
1.5	0.15705	0.01446	0.31409	0.02891	0.62819	0.05783	0.94228	0.08674	1.25637	0.11526
1.6	0.15617	0.01533	0.31234	0.03067	0.62468	0.06134	0.93701	0.09201	1.24935	0.12208
1.7	0.15530	0.01620	0.31060	0.03240	0.62120	0.06481	0.93181	0.09721	1.24241	0.12952
1.8	0.15444	0.01706	0.30889	0.03412	0.61777	0.06824	0.92666	0.10236	1.23554	0.13649
1.9	0.16360	0.01701	0.30710	0.03582	0.61438	0.07164	0.92166	0.10746	1.22876	0.14338
2.1	0.15192	0.01958	0.30385	0.03916	0.60770	0.07832	0.91154	0.11748	1.21539	0.15654

1. Table of Mass flow rates provided by CEQUEL.

	Mach #	0.05		0.1			
	φ	AIR	FUEL	AIR	FUEL	ΔP	Fuel_cor
Actual Conditions, Air Choke 0.236, Fuel Choke 0.157	0.8	337.5	32.7	689.7	80.0	28.5	108.5
	0.9	335.5	38.3	685.6	91.2	31.9	123.1
	1.0	333.4	43.8	681.6	102.3	35.0	137.3
	1.1	331.4	49.3	677.6	113.3	38.0	151.3
	1.2	329.4	54.7	673.6	124.1	40.8	164.9
	1.3	327.5	60.1	669.7	134.8	43.4	178.2
	1.4	325.6	65.4	665.8	145.4	45.9	191.3
	1.5	323.6	70.6	662.0	155.9	48.2	204.1
	1.6	321.8	75.8	658.2	166.3	50.4	216.6
	1.7	319.9	80.9	654.5	176.5	52.4	228.9
	1.8	318.0	86.0	650.8	186.6	54.3	240.9
	1.9	316.2	91.0	647.1	196.7	56.0	252.7
	2.1	312.6	100.8	639.9	216.4	59.1	275.5

2. Table of Air and Corrected Fuel Pressures Input to the ER3000.
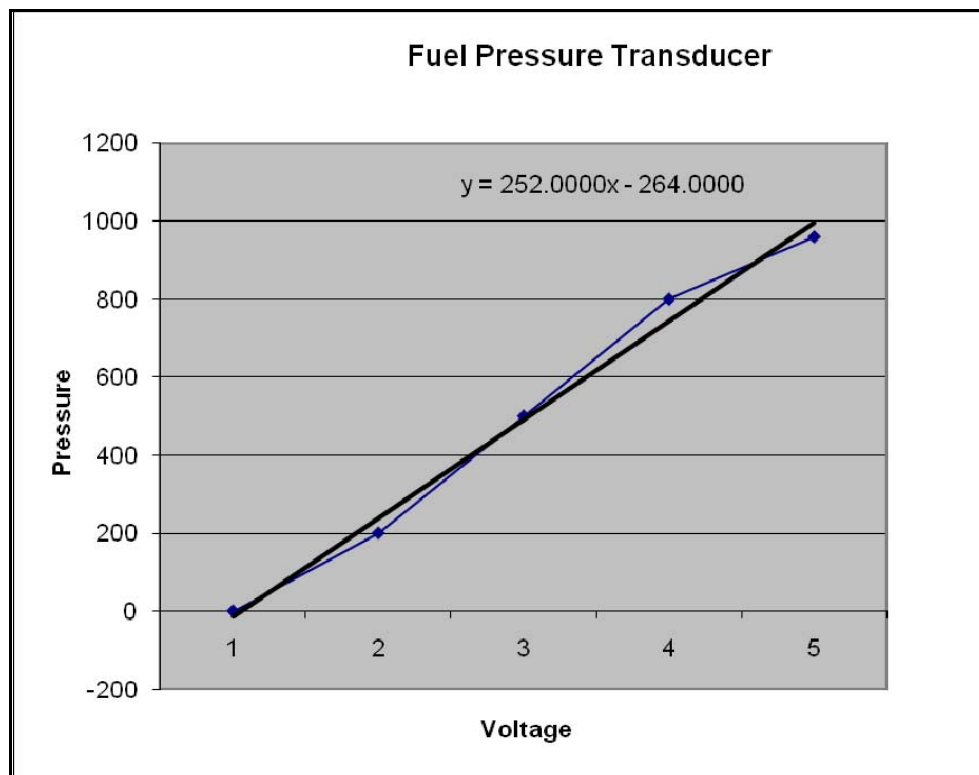
3. Fuel Pressure Transducer Calibration Curve for Fuel Pressure Correction.

Air Pressure Transducer

$$y = 240.0000x - 240.0000$$
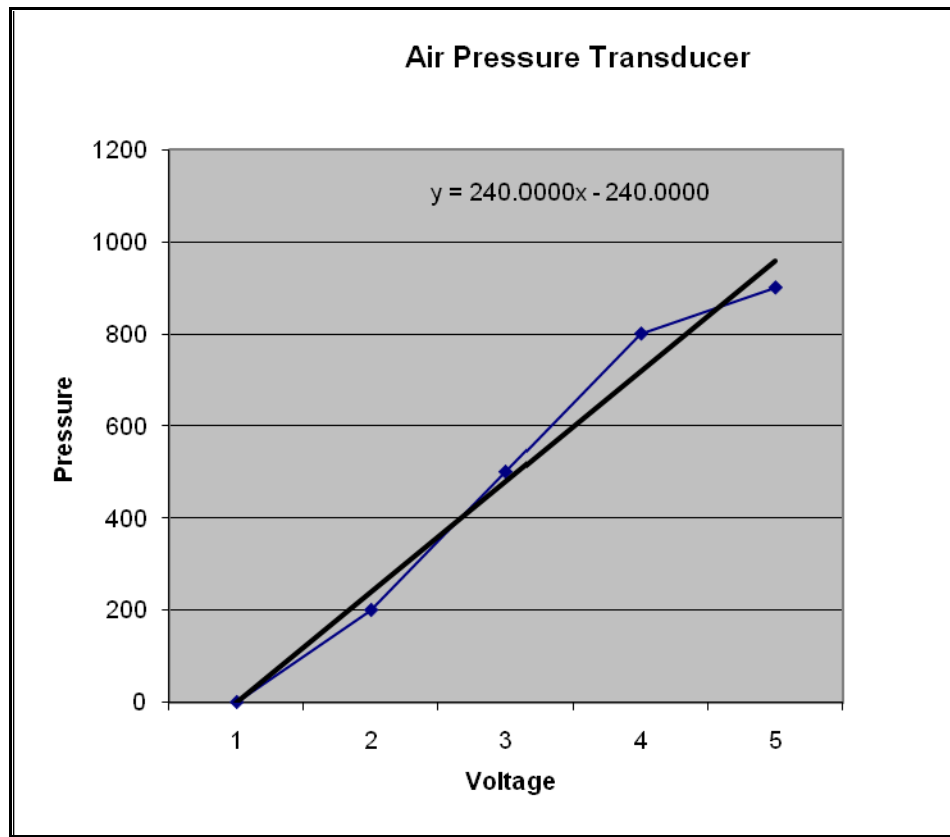
4. Air Pressure Transducer Calibration Curve for Air Pressure Correction.

APPENDIX D: STANDARD OPERATING PROCEDURE

Test Cell #1Standard Operating Procedures (S.O.P)
Combustor Start Up
(Modification Date 28 Oct 2009)

INITIAL PREPARATIONS

1. Notify all lab personnel of intention to make test cell 1 live.
2. Turn **ON** control console
3. Turn **ON** warning lights
4. Cell #1 EMERGENCY SHUTDOWN BUTTON (Control Room)- **VERIFY IN**
5. Notify the Golf Course (x2167) (Only required if Hot Fire Test is conducted)
6. Open Test Cell Door
7. Igniter Control (Test Cell)-**VERIFY OFF** (Red Button Out)
8. PXI-1000B Rack (Test Cell)-**VERIFY ON**
9. Shop Air-**VERIFY > 100 PSI**
10. Shop Air Valve (Test Cell)-**VERIFY OPEN**
11. 115 VAC Control/Cell #1 Switch (Control Room)-**ON**
12. 28VDC Power Supply/Cell #1 Switch (Control Room)-**ON**
13. Open LABVIEW

TESTING SET-UP

1. Viewing Section-Disconnect from Fill Tube (Includes unbolting ski ramps)

Note: Viewing Section must be removed and slid aft in order to continue

2. Install the ramp obstacles
3. Viewing Section-Attach to Fill Tube and bolt down ski ramps
4. Kistler Amplifier Power-**ENSURE OFF**
5. Kistler Leads-**CONNECT**
6. Exhaust Tube-**VERIFY PROPER POSTION**
7. Notify all personnel that gasses and TESCOM will be enabled.
8. Test Cell #2 and #3 Node 1 Air Isolation Valve (Test Cell #2)-**VERIFY CLOSED**

NOTE: This valve maybe left open only if Test Cell #2 or #3 is configured for active testing

9. Turn on Optical Sensor.
10. TRANSDUCER and TESCOM Power Switch (Test Cell #2)-**ON**

11. Set **0 (Zero)** pressures on ER3000 (Control Room) for the following:
    a. **Node 3 (Ethylene)**
    b. **Node 1 (Main Air)**
12. Main HP Air Jamesbury Valve (Outside Test Cell)-**OPEN SLOWLY**
13. Power Strip (above PXI-1000B)-**VERIFY ON**
14. Igniter Control Light (Red LED upper left on CRYDOM in PX-1000B Rack)-**VERIFY OUT**

DANGER: IF RED LIGHT IS ENERGIZED, MUST CLEAR USING LABVIEW BEFORE CONTINUING TO PREVENT PREMATURE IGNITION

15. Igniter Control (Test Cell)-**PUSH RED BUTTON IN**
16. Igniter Control Startup Diagnostics-**OBSERVE COMPLETION OF DIAGNOSTICS** (Verify energy level setting reads 2.03 J)
17. Main HP Air Isolation Valves (2) (Located in Test Cell)-**OPEN SLOWLY**

DANGER: OPEN VALVES SLOWLY TO PREVENT RAPID PRESSURIZTION OF DOWNSTREAM LINES

18. Node 3 (Ethylene) Shop Air Valve (Above Bottle in Bottle Room)-**OPEN**
19. Ethylene Bottle Isolation Valve (On Bottle)-**OPEN SLOWLY**

** VERIFY ADEQUATE ETHYLENE PRESSURE FOR TESTING ON DOWNSTREAM GAGE LOCATED IN BOTTLE ROOM**

PRE-TESTING

1. ULTRA Camera-**TURN ON AND REMOVE COVER**
2. Start ULTRA Software
3. Verify Image on ULTRA Software
4. Verify Desired Trigger Types and Valve Durations
5. Determine Desired Fuel and Air Pressures (Mass Flow Choke Calibrations.xls)
6. Set Required Pressures on ER3000
    a. **Node 3 (Ethylene)**
    b. **Node 1 (Main Air)**
7. Insert Tape into VCR
8. Switch Monitor to B (Test Cell #1)

TESTING

1. Clear All Test Cells and Verify with Head Count
2. Flashing Red Light and Siren-**ENERGIZE**
3. Verify Golf Course is **CLEAR**
4. VCR-**RECORD**
5. Camera-**ARM**

6. In LABVIEW Enable Facility Button-**ON**
7. Test Cell #1 Emergency Shutdown Button-**TURN CLOCKWISE**
8. In LABVIEW Start Button-**CLICK TO START**

WHEN TESTING COMPLETE

9. Set Node 1 Pressure to **0 (Zero)**
10. In LABVIEW Turn Off Button-**CLICK TO SECURE**
11. In LABVIEW Enable Facility Button-**VERIFY OFF**
12. Test Cell #1 Emergency Shutdown Button-**PUSH IN**
13. Siren-**OFF**
14. VCR-**Stop/Pause**
15. Save ULTRA Image

NOTE: If Further Testing is Required, re-perform steps 1-15 of the Testing Section

POST-TESTING

1. Set ER300 Node 3 (Ethylene) to **0 (Zero)**
2. Verify pressures on ER3000 are set to 0 (Zero) on the following:
   a. **Node 3 (Ethylene)**
   b. **Node 1 (Main Air)**
3. Main HP Air Isolation Valves (2) (Located in Test Cell)-**CLOSE**
4. Main HP Air Jamesbury Valve (Outside Test Cell)-**CLOSE**
5. Ethylene Bottle Isolation Valve (On Bottle)-**CLOSE**
6. Igniter Control (Test Cell)-**PUSH RED BUTTON OUT**

NOTE: If Further Testing will be accomplished with a different Ramp obstacle configuration, return to the TESTING SET-UP Section. If not continue to step 7.

7. ULTRA Camera-**TURN OFF AND INSTALL COVER**
8. TRANSDUCER and TESCOM Power Switch (Test Cell #2)-**OFF**
9. Close Test Cell Door
10. Node 3 (Ethylene) Shop Air Valve (Above Bottle in Bottle Room)-**CLOSE**
11. Secure Bottle Room
12. Exit out of ULTRA
13. EXIT out of LABVIEW
14. 28VDC Power Supply/Cell #1 Switch (Control Room)-**OFF**
15. 115 VAC Control/Cell #1 Switch (Control Room)-**OFF**

THIS PAGE INTENTIONALLY LEFT BLANK

APPENDIX E: TEST SUMMARY

Date	φ	Wavespeed (m/s)		Obstacle Configuration
9/30/2009			**Bad Data**	6 rows of 2
9/30/2009	1.13	2208.7		6 rows of 2
9/30/2009			**Bad Data**	6 rows of 2
9/30/2009			**Bad Data**	6 rows of 2
9/30/2009	1.32	2309.1		6 rows of 2
9/30/2009	1.33	4618.2		6 rows of 2
9/30/2009			**Bad Data**	6 rows of 2
9/30/2009	1.25	1881.5		6 rows of 2
9/30/2009	1.23	423.3		6 rows of 2
9/30/2009	1.33	1539.4		6 rows of 2
9/30/2009	1.39	1539.4		6 rows of 2
9/30/2009	1.14	2032		6 rows of 2
9/30/2009	1.46		**Bad Data**	6 rows of 2
9/30/2009	1.5		**Bad Data**	6 rows of 2
9/30/2009	1.46	1036.7		6 rows of 2
9/30/2009	1.41	2032		6 rows of 2
9/30/2009			**Bad Data**	6 rows of 2

Date	φ	Wavespeed (m/s)		Obstacle Configuration
10/2/2009			**Bad Data**	8 rows of 2
10/2/2009			**Bad Data**	8 rows of 2
10/2/2009			**Bad Data**	8 rows of 2
10/2/2009	1.13		**Bad Data**	8 rows of 2
10/2/2009	1.08	2309.1		8 rows of 2
10/2/2009	1.04	2309		8 rows of 2
10/2/2009			**No Data**	8 rows of 2
10/2/2009	1.01	2540		8 rows of 2
10/2/2009	0.95	2309		8 rows of 2
10/2/2009			**Bad Data**	8 rows of 2
10/2/2009	1.68	2674		8 rows of 2
10/2/2009	1.61	4233.3		8 rows of 2
10/2/2009	1.52	1539.4		8 rows of 2
10/2/2009	1.45	8466.7		8 rows of 2
10/2/2009			**Bad Data**	8 rows of 2
10/2/2009	1.64	2419.05		5 rows of 2 and 3 inline on the center
10/2/2009			**Bad Data**	5 rows of 2 and 3 inline on the center

Date	φ	Wavespeed (m/s)		Obstacle Configuration
10/6/2009	1.64	2674		5 rows of 2 and 3 inline on the center
10/6/2009	1.77	2419		5 rows of 2 and 3 inline on the center
10/6/2009			Bad Data	5 rows of 2 and 3 inline on the center
10/6/2009	1.53	2540		5 rows of 2 and 3 inline on the center
10/6/2009	1.46		Bad Data	5 rows of 2 and 3 inline on the center
10/6/2009			Bad Data	5 rows of 2 and 3 inline on the center
10/6/2009			Bad Data	5 rows of 2 and 3 inline on the center
10/6/2009	1.37	2540		5 rows of 2 and 3 inline on the center
10/6/2009	1.27	2540		5 rows of 2 and 3 inline on the center
10/6/2009	1.17	2419		5 rows of 2 and 3 inline on the center
10/6/2009			Bad Data	5 rows of 2 and 3 inline on the center
10/6/2009	1.04	2309		5 rows of 2 and 3 inline on the center
10/6/2009	0.94	2117		5 rows of 2 and 3 inline on the center
10/6/2009			Bad Data	5 rows of 2 and 3 inline on the center

Date	φ	Wavespeed (m/s)		Obstacle Configuration
10/6/2009	1.72	2309		4 rows of 2 and 3 inline on the center
10/6/2009	1.71	2309		4 rows of 2 and 3 inline on the center
10/6/2009	1.62	2419		4 rows of 2 and 3 inline on the center
10/6/2009	1.51	2419		4 rows of 2 and 3 inline on the center
10/6/2009	1.43	2674		4 rows of 2 and 3 inline on the center
10/6/2009	1.34	2540		4 rows of 2 and 3 inline on the center
10/6/2009	1.25	2674		4 rows of 2 and 3 inline on the center
10/6/2009	1.16	2419		4 rows of 2 and 3 inline on the center
10/6/2009	1.07	2419		4 rows of 2 and 3 inline on the center
10/6/2009	1.06	2309		4 rows of 2 and 3 inline on the center
10/6/2009	1.01	2309		4 rows of 2 and 3 inline on the center
10/6/2009	0.9	1881		4 rows of 2 and 3 inline on the center
10/6/2009	0.8			4 rows of 2 and 3 inline on the center
10/6/2009	1.71	2209		3 rows of 2 and 3 inline on the center
10/6/2009			Bad Data	3 rows of 2 and 3 inline on the center
10/6/2009	1.6	2117		3 rows of 2 and 3 inline on the center
10/6/2009	1.53	2419		3 rows of 2 and 3 inline on the center
10/6/2009	1.51		Bad Data	3 rows of 2 and 3 inline on the center
10/6/2009	1.41	2309		3 rows of 2 and 3 inline on the center
10/6/2009			Bad Data	3 rows of 2 and 3 inline on the center
10/6/2009	1.42	2419		3 rows of 2 and 3 inline on the center
10/6/2009	1.34	2540		3 rows of 2 and 3 inline on the center
10/6/2009	1.25	2419		3 rows of 2 and 3 inline on the center
10/6/2009	1.17	2540		3 rows of 2 and 3 inline on the center
10/6/2009	1.09	2117		3 rows of 2 and 3 inline on the center
10/6/2009	0.99	2032		3 rows of 2 and 3 inline on the center
10/6/2009			Bad Data	3 rows of 2 and 3 inline on the center

Date	φ	Wavespeed (m/s)		Obstacle Configuration
10/8/2009	1.76	2309		6 Rows Inline Top/Bottom
10/8/2009	1.68	2117		6 Rows Inline Top/Bottom
10/8/2009	1.6	2419		6 Rows Inline Top/Bottom
10/8/2009	1.5	2309		6 Rows Inline Top/Bottom
10/8/2009	1.42	2209		6 Rows Inline Top/Bottom
10/8/2009	1.32	2419		6 Rows Inline Top/Bottom
10/8/2009			**Bad Data**	6 Rows Inline Top/Bottom
10/8/2009	1.64	2117		5 Rows Inline Top/Bottom
10/8/2009	1.73	2309		5 Rows Inline Top/Bottom
10/8/2009	1.55	2209		5 Rows Inline Top/Bottom
10/8/2009	1.46		**Bad Data**	5 Rows Inline Top/Bottom
10/8/2009	1.37	2309		5 Rows Inline Top/Bottom
10/8/2009	1.3	2117		5 Rows Inline Top/Bottom
10/8/2009	1.23	2309		5 Rows Inline Top/Bottom

** Bad Data Was Due to Faulty Kistler Pressure Transducers

THIS PAGE INTENTIONALLY LEFT BLANK

LIST OF REFERENCES

[1]   R. Friedman, "American Rocket Society," Vol. 24, p.349, November 1953.

[2]   K.K. Kuo, *Principles of Combustion*, 2nd ed., John Wiley & Sons, Inc., 2005.

[3]   A. J. Higgins, P. Pinard, A. C. Yoshinaka, and J. H. S. Lee, "Sensitization of Fuel-Air Mixtures for Deflagration-to-Detonation Transition," in G. Roy, S. Frolov, D. Netzer, and A. Borisov (Eds.), *High-Speed Deflagration and Detonation: Fundamentals and Control*, pp. 45–49, ELEX-KM Publishers, 2001.

[4]   Patrick D. Hutcheson, Design, *Modeling and Performance of a Split Path JP-10/Air Pulse Detonation Engine*, M.S. Thesis, Naval Postgraduate School, Monterey, CA, December 2006.

[5]   Michael A. Fludovich Jr., *Investigation of Detonation Wave Diffraction Interaction with Reactive Transpiration*, M.S. Thesis, Naval Postgraduate School, Monterey CA, September 2002.

[6]   Michael A. Fludovich Jr., "Pulsed Detonation Engines: Investigation of Detonation Wave Diffraction with Reactive Transpiration," Master's Thesis Presentation, Monterey, CA, September 2002.

[7]   John A. Anderson, D*eflagration-to-Detonation Transition Enhancement Using Low-Loss Obstacle Fields,* M.S. Thesis, Naval Postgraduate School, Monterey, CA, December 2007.

[8]   Carlos A. Medina, *Evaluation of Straight and Swept Ramp Obstacles on Enhancing Deflagration to Detonation Transition in Pulse Detonation Engines*, M.S. Thesis, Naval Postgraduate School, Monterey, CA, December 2006.

[9]   Ultra 17 High-Speed Imaging System Data Sheet, DRS Data & Imaging Systems, Inc.

[10]   R. P. Benedict, Fundamentals of Temperature, Pressure and Flow Measurements, John Wiley & Sons, Inc., 1984.

[11]   B. Varatharajan, M. Petrova, and F. Williams, "Two-Step Chemical-kinetic descriptions for Hydrocarbon-Oxygen-Diluent Ignition and Detonation Applications," Presentation to the 30th International Symposium on Combustion, December 2003.

[12]   B. T. Channell, *Evaluation and Selection of an Efficient Fuel/Air Initiation Strategy for Pulse Detonation Engines*, M.S. Thesis, Naval Postgraduate School, Monterey, CA, September 2005.

[13]   Patrick D. Hutcheson, et. al., "Investigation of Flow Field Properties on Detonation Initiation," Presentation to the 42nd AIAA/ASME/SAE/ASEE Joint Propulsion Conference, July 2006.

[14]   Micro Switch 140PC30 Series Pressure Transducer Data Sheet, Honeywell, Inc.

INITIAL DISTRIBUTION LIST

1.   Defense Technical Information Center
      Ft. Belvoir, Virginia

2.   Dudley Knox Library
      Naval Postgraduate School
      Monterey, California

3.   Professor Christopher Brophy
      Department of Mechanical and Astronautical Engineering
      Monterey, California

4.   Professor Garth Hobson
      Department of Mechanical and Astronautical Engineering
      Monterey, California

5.   Professor Knox Millsaps
      Department of Mechanical and Astronautical Engineering
      Monterey, California

6.   LT Charles Myers
      Naval Postgraduate School
      Monterey, California